



Contents lists available at ScienceDirect

Ore Geology Reviews

journal homepage: www.elsevier.com/locate/oregeo

Mineralogy, fluid inclusions, and isotopes of the Cihai iron deposit, eastern Tianshan, NW China: Implication for hydrothermal evolution and genesis of subvolcanic rocks-hosted skarn-type deposits

Jiahao Zheng ^{a,b,c,*}, Jingwen Mao ^b, Fuquan Yang ^b, Fengmei Chai ^d, Yongfeng Zhu ^{a,*}^a Key Laboratory of Orogenic Belts and Crustal Evolution, Ministry of Education, School of Earth and Space Sciences, Peking University, Beijing 100871, China^b MLR Key Laboratory of Metallogeny and Mineral Assessment, Institute of Mineral Resources, Chinese Academy of Geological Sciences, 26 Baiwanzhuang Road, Beijing 100037, China^c Key Laboratory of Mineral Resources, Institute of Geology and Geophysics, Chinese Academy of Sciences, Beijing 100029, China^d Xinjiang Key Laboratory for Geodynamic Processes and Metallogenesis of the Central Asian Orogenic Belt, College of Geology and Mining Engineering, Xinjiang University, Urumqi 830049, China

ARTICLE INFO

Article history:

Received 15 November 2016

Received in revised form 19 January 2017

Accepted 24 January 2017

Available online 28 February 2017

Keywords:

Mineralogy

Isotopes

Fluid inclusions

Cihai iron deposit

Subvolcanic rocks-hosted skarn deposit

ABSTRACT

Most skarn deposits are closely related to granitoids that intruded into carbonate rocks. The Cihai (>100 Mt at 45% Fe) is a deposit with mineral assemblages and hydrothermal features similar to many other typical skarn deposits of the world. However, the iron orebodies of Cihai are mainly hosted within the diabase and not in contact with carbonate rocks. In addition, some magnetite grains exhibit unusual relatively high TiO₂ content. These features are not consistent with the typical skarn iron deposit. Different hydrothermal and/or magmatic processes are being actively investigated for its origin. Because of a lack of systematic studies of geology, mineral compositions, fluid inclusions, and isotopes, the genetic type, ore genesis, and hydrothermal evolution of this deposit are still poorly understood and remain controversial.

The skarn mineral assemblages are the alteration products of diabase. Three main paragenetic stages of skarn formation and ore deposition have been recognized based on petrographic observations, which show a prograde skarn stage (garnet-clinopyroxene-disseminated magnetite), a retrograde skarn stage (main iron ore stage, massive magnetite-amphibole-epidote ± ilvaite), and a quartz-sulfide stage (quartz-calcite-pyrite-pyrrhotite-cobaltite).

Overall, the compositions of garnet, clinopyroxene, and amphibole are consistent with those of typical skarn Fe deposits worldwide. In the disseminated ores, some magnetite grains exhibit relatively high TiO₂ content (>1 wt.%), which may be inherited from the diabase protoliths. Some distinct chemical zoning in magnetite grains were observed in this study, wherein cores are enriched in Ti, and magnetite rims show a pronounced depletion in Ti. The textural and compositional data of magnetite confirm that the Cihai Fe deposit is of hydrothermal origin, rather than associated with iron rich melts as previously suggested.

Fluid inclusions study reveal that, the prograde skarn (garnet and pyroxene) formed from high temperature (520–600 °C), moderate- to high-salinity (8.1–23.1 wt.% NaCl equiv, and >46 wt.% NaCl equiv) fluids. Massive iron ore and retrograde skarn assemblages (amphibole-epidote ± ilvaite) formed under hydrostatic condition after the fracturing of early skarn. Fluids in this stage had lower temperature (220°–456 °C) and salinity (8.4–16.3 wt.% NaCl equiv). Fluid inclusions in quartz-sulfide stage quartz and calcite also record similar conditions, with temperature range from 128° to 367 °C and salinity range from 0.2 to 22.9 wt.% NaCl equiv. Oxygen and hydrogen isotopic data of garnet and quartz suggest that mixing and dilution of early magmatic fluids with external fluids (e.g., meteoric waters) caused a decrease in fluid temperature and salinity in the later stages of the skarn formation and massive iron precipitation. The δ¹⁸O values of magnetite from iron ores vary between 4.1 and 8.5‰, which are similar to values reported in other skarn Fe deposits. Such values are distinct from those of other iron ore deposits such as Kiruna-type and magmatic Fe-Ti-V deposits worldwide. Taken together, these geologic, geochemical, and isotopic data confirm that Cihai is a diabase-hosted skarn deposit related to the granitoids at depth.

© 2017 Elsevier B.V. All rights reserved.

* Corresponding authors at: Key Laboratory of Orogenic Belts and Crustal Evolution, Ministry of Education, School of Earth and Space Sciences, Peking University, Beijing 100871, China

E-mail addresses: joey-zen@163.com (J. Zheng), yfzhu@pku.edu.cn (Y. Zhu).

1. Introduction

Most traditional skarn Fe deposits are closely related to granitoids that intruded into carbonate rocks (Meinert et al., 2005), and several studies have addressed the genesis and evolution of iron skarns (e.g., Meinert, 1984; Zürcher et al., 2001; Pons et al., 2009; Xie et al., 2012; Jansson and Allen, 2013). Non-traditional skarn deposits hosted in volcanic and subvolcanic rocks have also been reported (e.g., Rose et al., 1985; Jiang et al., 2014; Li et al., 2015), but the genesis and hydrothermal evolution of this type skarn deposit remains subject to debate. Magnetite from skarn and other hydrothermal iron deposits worldwide are characterized by low-Ti content (Dupuis and Beaudoin, 2011; Zhang et al., 2014a). However, most recently, some magnetites with high-Ti content have been reported in some iron skarn deposits (Hu et al., 2015). Due to lack of a link between compositional data and detailed geological background, the genesis and evolution of these high-Ti magnetites are still uncertain.

The Tianshan orogenic belt is considered to be one of the most important iron ore belts in China (Zhang et al., 2014b, 2015). It hosts numerous iron deposits and occurrences, several of which contain ore reserves >100 million metric tons (Mt). Many of these iron deposits have well-developed skarn-type mineral assemblages. Recent researches have documented the geological characteristics, isotopic ages, genesis of ores and associated felsic rocks, as well as tectonic setting of these iron deposits (e.g., Mao et al., 2005; Hong et al., 2012; Hou et al., 2013; Duan et al., 2013; Jiang et al., 2014; Huang et al., 2014; Zhu et al., 2009). However, the hydrothermal evolution of these iron deposits is poorly constrained, and their origin remains controversial.

Located in the eastern Tianshan, the Cihai deposit is one of the largest iron deposits (>100 Mt at 45% Fe) in the Tianshan orogenic belt. It is spatially associated with the diabase and has well-developed skarn-type mineral assemblages. In addition, some magnetites with

relatively high Ti content were reported in the Cihai deposit (>1% wt. %; Wang et al., 2006). Thus, it provides an excellent opportunity to understand the hydrothermal evolution of subvolcanic rocks related skarn deposit as well as the genesis of relatively high Ti magnetites in skarn. Moreover, the good outcrops of the Cihai iron deposit make this an ideal region to shed light on the genetic model for this type of deposit. Over the past three decades, several studies have been carried out on the Cihai Fe deposit, most of which focused on the age, geochemistry, and genesis of the iron ore-hosted diabase (Xue et al., 2000; Hou et al., 2013; Zheng et al., 2015). However, due to lack of systematic studies of detailed geology, mineral compositions, fluid inclusions, and stable isotopes, many issues, including the genesis and hydrothermal evolution of Cihai Fe deposit are still debated. Some authors believe it formed from iron oxide magma because the iron orebodies were hosted in the diabase and some magnetite ore bodies have sharp contact with host diabase (Sheng, 1985; Zhao, 2000; Wang et al., 2006; Tang et al., 2010). By contrast, based on the widespread metasomatic alteration at Cihai, other researchers propose that Cihai is a hydrothermal deposit (Hou et al., 2013; Huang et al., 2013).

Here, we use geological observation together with silicate mineral composition, textural and compositional data for magnetite, fluid inclusions, and the composition of H-O isotopes to constrain the source for fluids and ore metals of the Cihai Fe deposit, and to provide new insight into the genesis and evolution for subvolcanic rocks-hosted skarn deposit as well as the origin of high-Ti magnetite.

2. Regional geology

Located between the Siberian Craton to the north and the Tarim-North China Craton to the south, the central Asian orogenic belt (CAOB; Fig. 1a) was formed by multiple subduction-accretion and collision processes from the Neoproterozoic to the late Paleozoic (e.g., Jahn et al., 2000; Windley et al., 2007; Kröner et al.,

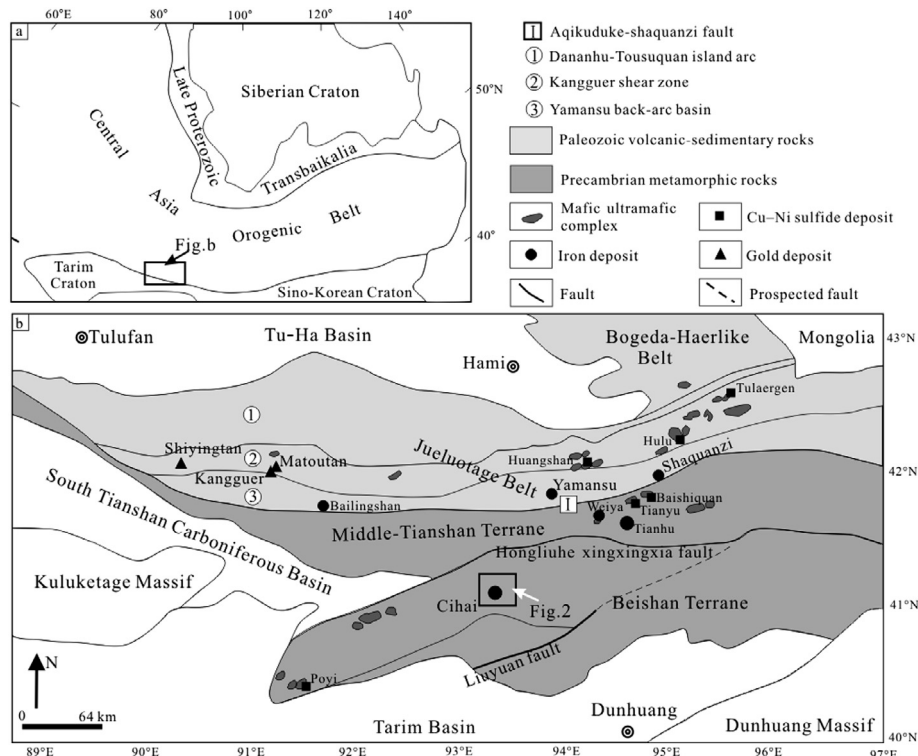


Fig. 1. (a) Geological map showing the location of eastern Tianshan in Central Asian Orogenic Belt. (b) Regional geological map of the eastern Tianshan showing the distribution of iron deposits, gold deposits, and mafic-ultramafic complexes (modified from Su et al., 2012; Wang et al., 2007).

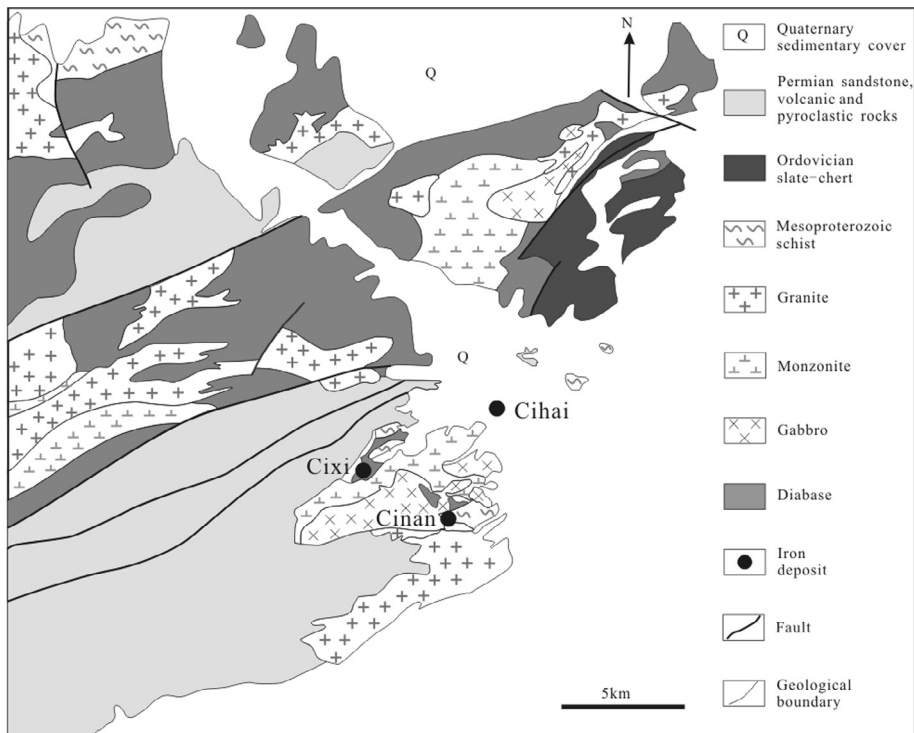


Fig. 2. Geological map of the Cihai (modified from geological report of No. 5 Geological Team, Geological Exploration Bureau of NW China).

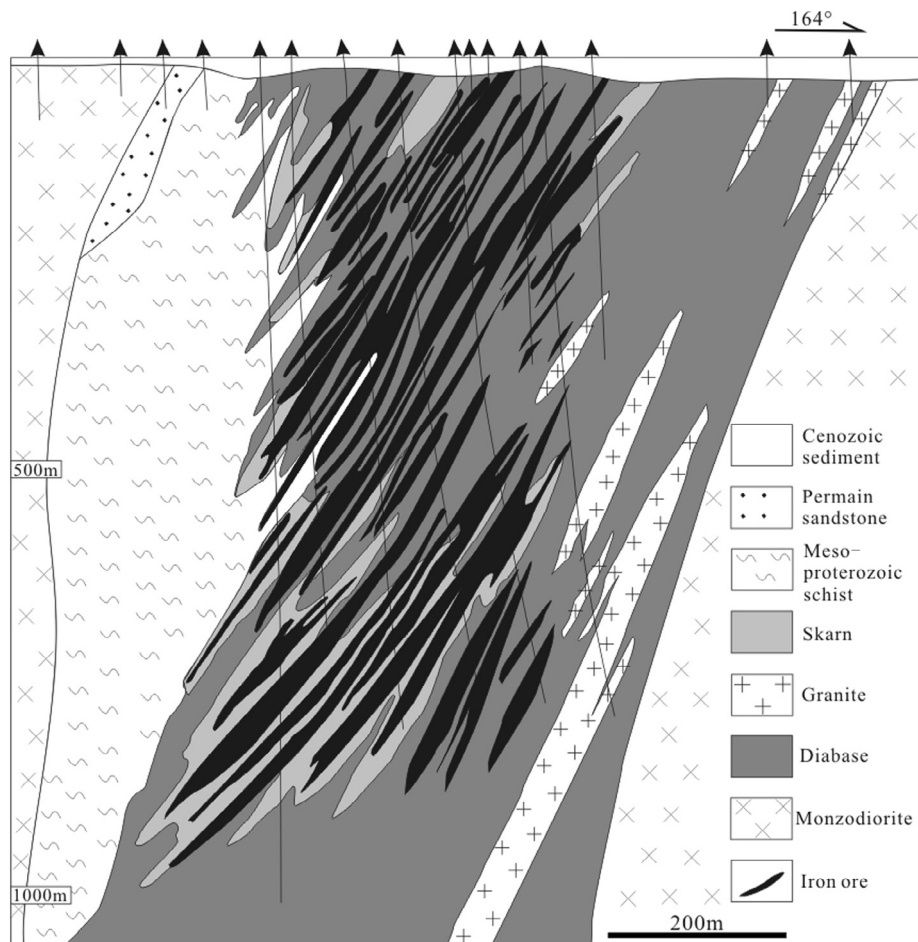


Fig. 3. Cross-section diagram of the Cihai iron deposit (modified from Xue et al., 2000).

2014), and hosts numerous base and precious metal deposits (e.g., Chai et al., 2009; Mao et al., 2008; Pirajno et al., 2008; Qin et al., 2011; Yang et al., 2013, 2014; Goldfarb et al., 2014; Zheng et al., 2016a,b; Zhu et al., 2016). The eastern Tianshan, situated in the southern part of the CAOB, is herein defined as all parts of the mountain range located east of the Urumuqi-Korla Road, and bounded by the southern margin of the Tuha basin and the northern margin of Tarim basin (Fig. 1b). It is composed of the Bogeda-Haerlike belt, the Jueluotage belt, the Middle Tianshan terrane, and the Beishan terrane. The Bogeda-Haerlike and Jueluotage belt are characterized by Paleozoic volcanic-sedimentary rocks, whereas the Middle Tianshan and Beishan terrane mainly comprise Proterozoic metamorphic rocks (Fig. 1b). Large volumes of Early Carboniferous to Early Permian granitic rocks outcrop in the eastern Tianshan (Zhou et al., 2010; Zheng et al., 2016c). The eastern Tianshan was formed by progressive accretion of different terranes during the middle to late Paleozoic (Xiao et al., 2004; Han et al., 2010). At ca. 600 Ma, the Junggar Ocean started to subduct toward

the Middle Tianshan and Beishan along the Bogeda-Haerlike Belt, and formed Bogeda-Haerlike island arcs and Yamansu back-arc basin. The subduction probably terminated in the Late Carboniferous, and subsequent orogenesis occurred between Late Carboniferous and Early Permian (Su et al., 2011).

The eastern Tianshan is characterized by a number of economic Cu-Ni sulfide, Au, and Fe deposits. The mafic-ultramafic complexes-related Cu-Ni sulfide deposits widely crop out in the eastern Tianshan, and mainly formed between 301 and 269 Ma (Mao et al., 2003; Qin et al., 2011). The gold deposits locate in the Jueluotage belt of the region and also formed during the Early Permian (Zheng et al., 2015). Iron deposits in the eastern Tianshan can be further divided into three major types: (1) Volcanic and subvolcanic rocks-hosted iron deposits, (2) Sedimentary-metamorphic iron deposit, and (3) Fe-Ti oxide deposit (Chen et al., 2008; Mao et al., 2005). The volcanic and subvolcanic rocks-hosted iron deposits include those at Bailingshan, Yamansu, Shaquanzi, and Cihai, whereas the sedimentary-metamorphic iron

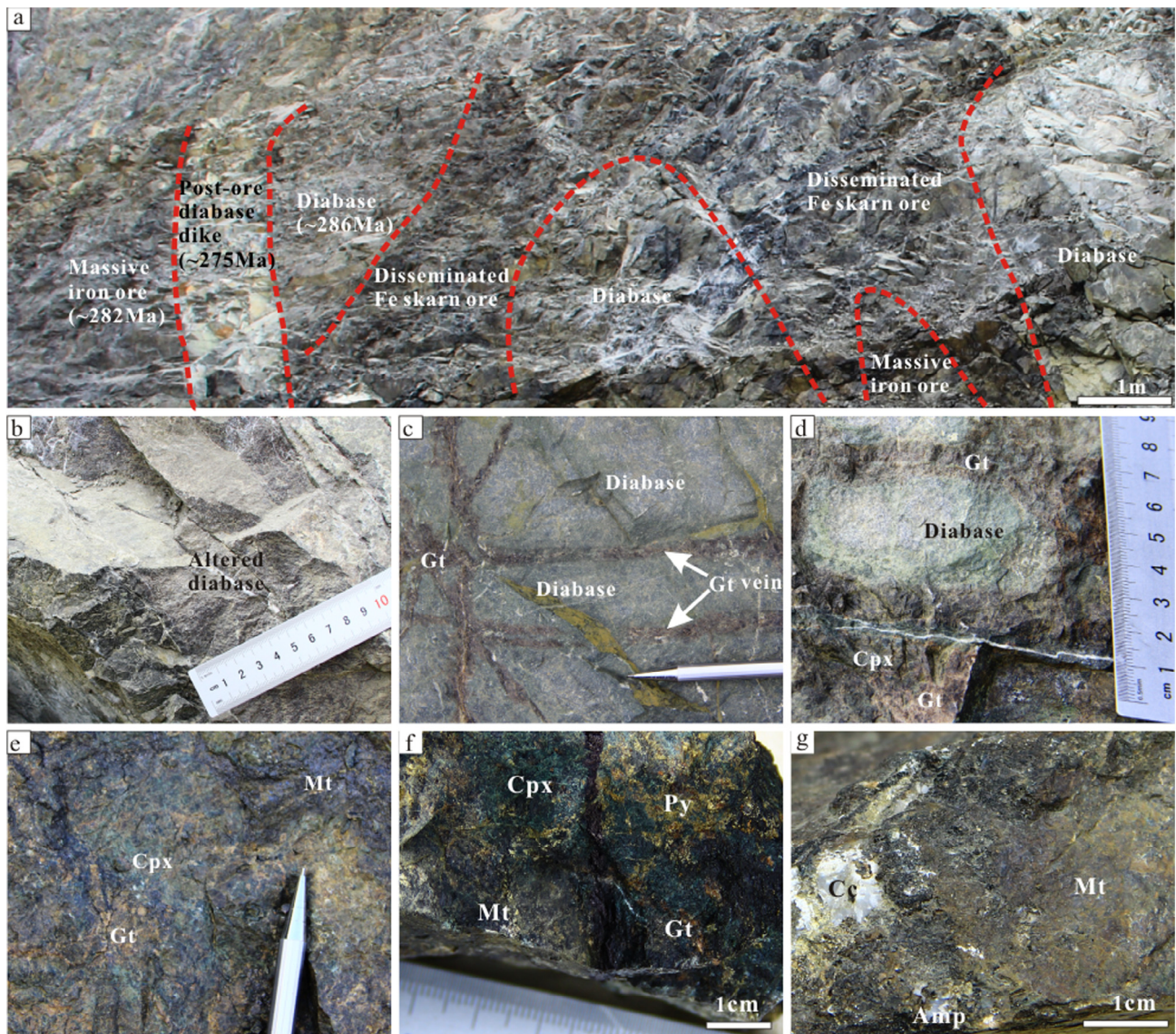


Fig. 4. (a) A representative photo showing spatial relations between ore-hosted diabase, disseminated Fe skarn, massive iron ores, and post-ore diabase dikes in the Cihai open pit. (b) Potassium-sodium alteration in diabase. (c) Garnet vein in the diabase. (d) Diabase was enclosed by garnet + clinopyroxene assemblage. (e) Garnet + clinopyroxene ± magnetite assemblage. (f) Disseminated mineralized skarn, dark green clinopyroxene + brown garnet + magnetite + pyrite. (g) Massive iron ore, abundant magnetite + amphibole + calcite. Mineral abbreviations: Cpx = clinopyroxene, Pl = plagioclase, Bi = biotite, Mt = magnetite, Cc = calcite, Amp = amphibole, Gt = garnet, Py = pyrite. (For interpretation of the references to colour in this figure legend, the reader is referred to the web version of this article.)

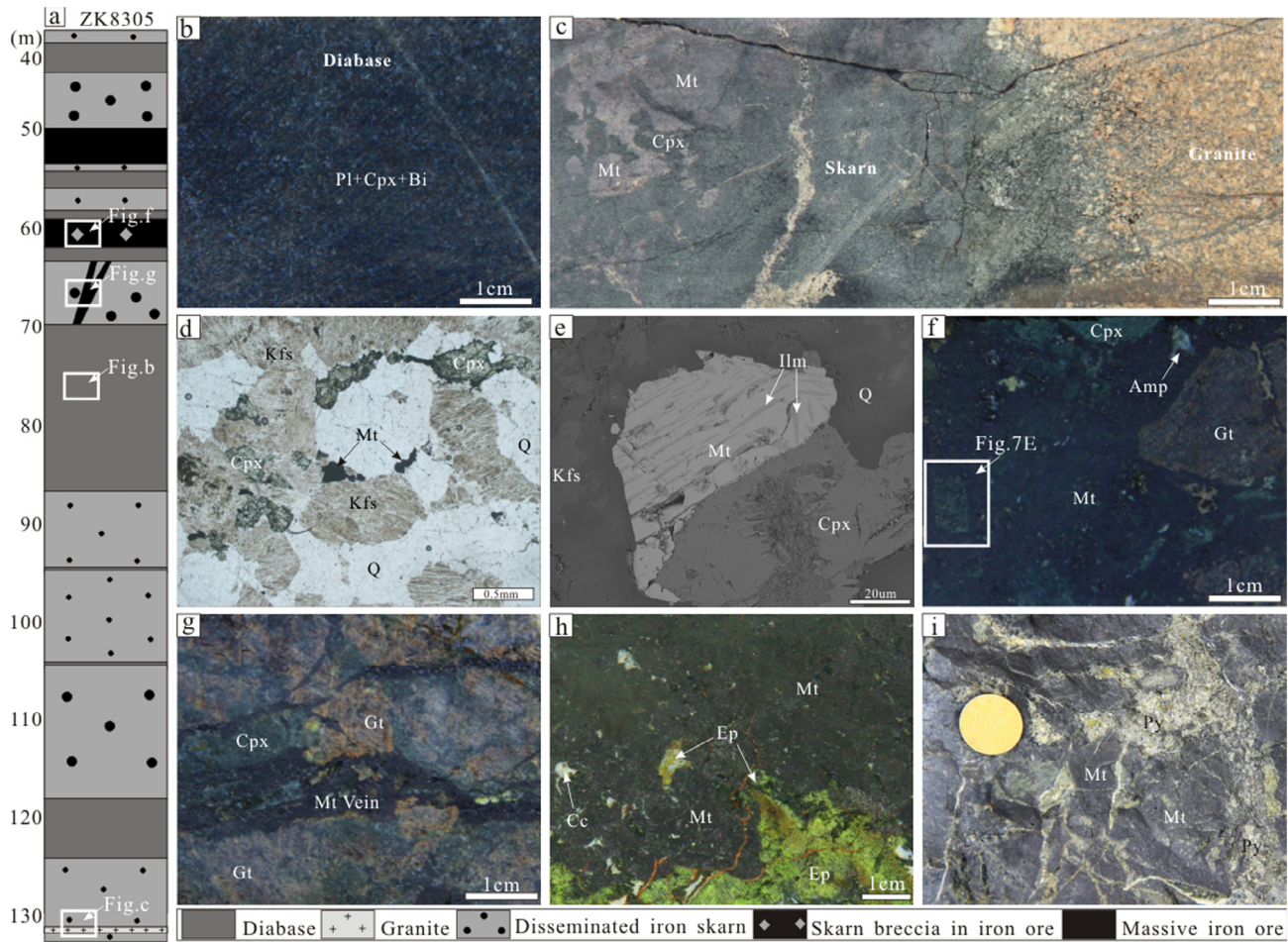


Fig. 5. Schematic profile of the Cihai drill hole and representative samples of the main alteration and mineralization styles in the deposit. (a) Schematic profile of the Cihai drill hole, showing the relationship between diabase, skarn, and iron ore. (b) The ore-hosted diabase, the clinopyroxene partly altered into biotite. (c) The spatial contact relation between granite and iron skarn. (d) The main minerals of granite are potassium feldspar, quartz, and clinopyroxene, with minor magnetite. (e) Ilmenite lamellae lying on the magnetite host in granite. (f) Skarn breccias are cemented by massive magnetite assemblage. (g) Magnetite vein crosscut early skarn. (h) Magnetite intergrowth with epidote in massive iron ore. (i) Pyrite vein crosscut massive iron ore. Mineral abbreviations: Cpx = clinopyroxene, Pl = plagioclase, Bi = biotite, Kfs = potassium feldspar, Q = quartz, Ilm = ilmenite, Gt = garnet, Mt = magnetite, Amp = amphibole, Ep = epidote, Py = pyrite.

deposit and Fe-Ti oxide deposit are represented by the Tianhu and Weiya, respectively (Fig. 1b). Located in the Middle Tianshan terrane, the Tianhu iron deposit (>104 Mt at 42% Fe) has a pyrite Re-Os age of ~530 Ma (Huang et al., 2015), whereas Fe-Ti oxide-bearing Weiya mafic intrusion has been dated at 236 Ma by zircon U-Pb method (Zhang et al., 2005). The Yamansu and Shaquanzi iron deposits in the Juelutage belt were formed between 324–300 Ma (324 Ma for the Yamansu by zircon U-Pb dating, Hou et al., 2014; ~300 Ma for the Shaquanzi by magnetite Re-Os dating, Huang et al., 2014). As one of the largest Fe deposits in the eastern Tianshan, the Cihai iron deposit (>100 Mt at 45% Fe) is situated in the Beishan terrane. Amphibole separated from massive iron ore gives a ^{40}Ar - ^{39}Ar plateau age of 281.9 ± 2.2 Ma (MSWD = 0.74; Zheng et al., 2015), which represents the time of massive iron ore formation at Cihai.

3. Geology of the Cihai magnetite deposit

The exposed rocks in the Cihai ore district include Mesoproterozoic metamorphic rocks, Ordovician slate and chert, and Permian sandstone, siltstone, volcanic and pyroclastic rocks (Fig. 2). The Mesoproterozoic metamorphics are exposed in the central parts of the ore district and hosts parts of the Cihai iron ore. The Ordovician slate and chert outcrop in the northeastern parts of the ore district. The Permian volcanic and pyroclastic rocks are exposed

in the western and northern ore district, and consist of andesite, dacite, basalt, tuff, and volcanic breccia. The Permian sandstone and siltstone outcrops in the western ore district.

The Cihai ore district is located between two regional deep-seated NW-SE striking faults as Hongliu-xingxingxia Fault and Liuyuan Fault (Fig. 1b). The area around the Cihai Fe deposit is characterized by NE-striking faults (Fig. 2). Intrusive rocks are exposed widely in the central parts of the Cihai ore district, and are predominantly composed of gabbro, monzonite, monzodiorite, and granite stocks, multiple pulses of diabase emplaced into monzodiorite and Mesoproterozoic strata. The diabase is the most common intrusive rock within the Cihai ore district, and is spatially associated with iron mineralization (Fig. 2). The orebodies of the Cihai Fe deposit are generally hosted in the diabase (Fig. 3), however, some late diabase dikes crosscut previously emplaced diabase as well as iron orebodies, indicating they were also emplaced after the formation of the orebodies (Fig. 4a). Some small granitoid dikes (~286–284 Ma; Zheng et al., 2016c) emplaced into diabase and formed disseminated iron skarn as shown in drillholes (Fig. 5c). The granitoid dikes mainly consist of feldspar, quartz, and clinopyroxene, with magnetite as accessory minerals (Fig. 5d), and ilmenite exsolution in magnetite has been recognized (Fig. 5e). Zheng et al. (2015) obtained zircon U-Pb age of iron ore hosting diabase in the ore district, yielding an age of 286.5 ± 1.8 Ma, and massive iron ore has an amphibole ^{40}Ar - ^{39}Ar plateau age of ~282 Ma. These

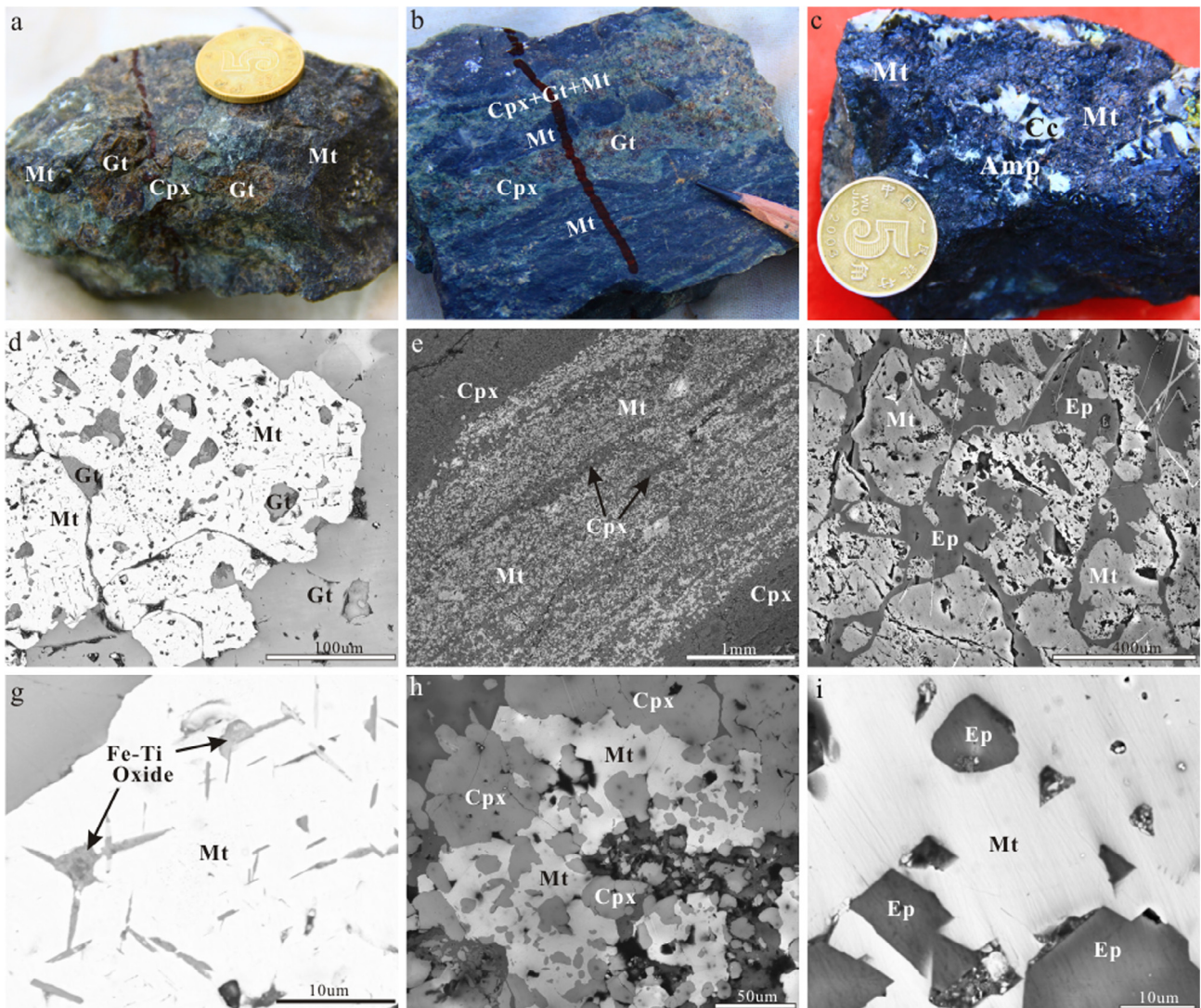


Fig. 6. Photographs showing major types of iron ores and magnetite characteristics in the Cihai deposit. (a) Disseminated magnetite in garnet-clinopyroxene skarn. (b) Banded ores with thin interbeds of clinopyroxene + garnet + minor magnetite assemblage and magnetite + clinopyroxene + minor garnet assemblage. (c) Massive ores associated with amphibole and calcite. (d) Disseminated magnetite grain in textural equilibrium with garnet, BSE. (e) Magnetite dominated band in banded ores, with minor clinopyroxene, BSE. (f) Massive iron ores, magnetite grain in textural equilibrium with epidote. (g) Closeup views for magnetite grains of (d), exsolution of Fe-Ti oxide in magnetite, BSE. (h) Closeup views for magnetite grains of (e), magnetite grains are homogeneous and in textural equilibrium with clinopyroxene, BSE. (i) Closeup views for magnetite grain of (f), magnetite grain is homogeneous and in textural equilibrium with epidote, BSE. Mineral abbreviations: Gt = garnet, Cpx = clinopyroxene, Mt = magnetite, Cc = calcite, Amp = amphibole, Ep = epidote.

data indicate that the Cihai iron skarn must have been formed between 286 and 282 Ma. Sulfides, which formed later than massive iron ores (Fig. 5i), have a wide error range for the Re-Os isochron age of 267 ± 30 Ma (Huang et al., 2013). The different post-ore diabase dikes give zircon U-Pb ages 275.8 ± 2.2 Ma or 128.5 ± 0.3 Ma (Hou et al., 2013; Zheng et al., 2015).

The Cihai iron deposit is divided into three mining sections: Cihai, Cixi and Cinan (Fig. 2). The Cihai mining section is the largest open pit located in the northeast of the district, the total resources are estimated at >100 Mt with an average grade of 45.7% (Wang et al., 2007), and comprises 90% of the iron ore reserve in the district, while the Cixi and Cinan section are relatively small in scale and are mining underground.

The magnetite ore bodies are usually lens-shaped, and mainly occur within the diabase with minor amounts in the contact zone between diabase and schist. In the Cihai mining section the monzodiorite was intruded by diabase, and the monzodiorite does not show any close spatial relations with iron ore bodies. The

pyroxene-garnet skarn are well developed in the diabase and spatially related to the iron ore bodies. The diabase was intruded by granite (Fig. 3).

In the Cihai open pit, massive iron ores are present within the garnet-pyroxene skarn or between the skarn and diabase (Fig. 4). The garnet-pyroxene skarns are exposed as parallel or nearly parallel bands, ranging from ~1 m to >10 m thick, adjacent to the diabase. The diabase is dark green (Fig. 4a) or dark brown (Fig. 5b). The skarn is mainly composed of garnet and pyroxene with varying amount of disseminated magnetite, and there is no obvious large-scale pyroxene-rich zone or garnet-rich zone. The massive, small-scale garnet-dominated skarn is brown red, whereas similar textured pyroxene-dominated skarn is dark green (Fig. 4f). The high grade massive magnetite ores consist of assemblages of magnetite + amphibole + calcite ± epidote (Figs. 4g and 5h).

The alteration characteristics in a drillhole section in the Cihai deposit are similar to those of the Cihai open pit (Fig. 5a). The drill

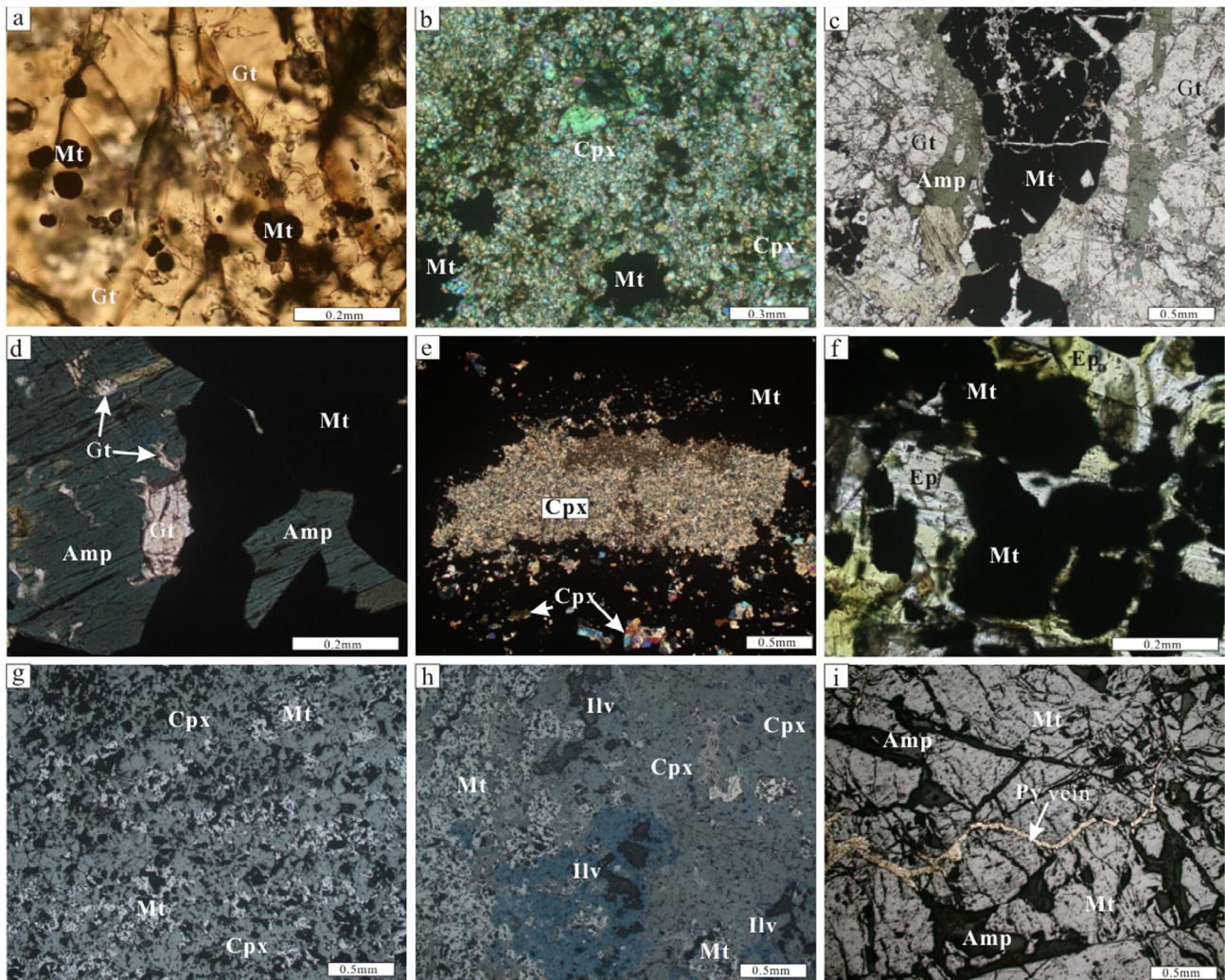


Fig. 7. Photomicrographs showing mineralization-related skarn minerals. (a) Disseminated magnetite grains in garnet. (b) Disseminated magnetite grains are interstitial to clinopyroxene. (c) Garnet was overprinted by amphibole. (d) Abundant amphibole replaced garnet, and amphibole are associate with massive magnetite. (e) Early formed clinopyroxene breccia was enclosed by massive magnetite. (f) Magnetite intergrowth with epidote in massive iron ore. (g) Disseminated magnetite grains are mainly interstitial to clinopyroxene. (h) Ilvaite replaced clinopyroxene and associated with the formation of magnetite. (i) Pyrite vein crosscut massive iron ore. Mineral abbreviations: Gt = garnet, Mt = magnetite, Cpx = clinopyroxene, Amp = amphibole, Ep = Epidote, Ilv = ilvaite, Py = pyrite.

hole consists of altered diabase hosting (Fig. 5b), disseminated magnetite in garnet-pyroxene mineral assemblage and massive ores. Some diabase experienced skarn alteration. Retrograde alteration overprints or crosscuts the early formed skarn and is closely associated with the massive iron ore (Figs. 5g and h). Both garnet-dominated and clinopyroxene-dominated skarn assemblages also appear as breccias, which are cemented by massive magnetite assemblage (Fig. 5f). Sulfide vein formed after massive iron ores (Fig. 5i).

4. Alteration, mineralization, and paragenesis

4.1. Alteration

The Cihai iron deposit is different from traditional skarn Fe deposits. As observed in the Cihai open pit and drill holes, the diabase has experienced various alteration. The alteration includes two types, K-Na alteration (Fig. 4b) and skarn-type alteration (Figs. 4c-e). The main K-Na alteration minerals are biotite and albite; Ca-rich plagioclase has undergone sodic alteration and clinopyroxene biotite alteration. It is noteworthy that there is no magnetite grains in the diabase, all iron oxides in fresh and altered

diabase are ilmenite. Skarn alteration in diabase evolved from garnet veins in the diabase (Fig. 4c), followed by garnet + clinopyroxene assemblage (Fig. 4d) by complete replacement by a garnet + clinopyroxene ± magnetite assemblage (Fig. 4e).

Most individual garnet crystals have relatively homogeneous compositions, whereas some garnet grains are anisotropic, and contain oscillatory zoning (Fig. 9a). Individual clinopyroxene crystals have relatively homogeneous compositions. Garnet and clinopyroxene grains are closely associated and in textural equilibrium with disseminated magnetite (Figs. 7a and 10a); whereas amphibole is closely associated and in textural equilibrium with massive magnetite (Fig. 10c).

4.2. Iron mineralization

The Cihai deposit mainly consists of three types of iron mineralization: (1) Disseminated magnetite in garnet-pyroxene skarn (Fig. 6a) where magnetite grains are closely associated and in textural equilibrium with garnet (Figs. 6d and 7a). Some orientated exsolution lamellae of Fe-Ti oxides in the low Ti magnetite are present in the disseminated iron ore (Fig. 6g). Clinopyroxene (Fig. 7b) and garnet was overprinted by amphibole (Fig. 7c). (2) Banded iron ores are characterized by thin interbeds of clinopyroxene + garnet

Mineral \ Stage	K-Na alteration	Prograde skarn	Retrograde skarn	Quartz-calcite -sulfide
Albite	—			
Biotite	—			
Diopside		—		
Hedenbergite		—		
Garnet	—	—		
Amphibole			—	
Chlorite			—	
Epidote			—	
Ilvaite			—	
Magnetite		—	—	—
Pyrrhotite			—	—
Pyrite			—	—
Chalcopyrite			—	—
Arsenopyrite			—	—
Native Gold			—	—
Native Bismuth			—	—
Maldonite			—	—
Hedleyite			—	—
Cobaltite			—	—
Safflorite			—	—
Quartz			—	—
Calcite			—	—

Fig. 8. Paragenetic sequence of minerals in the Cihai Fe deposit.

+ minor magnetite and magnetite + clinopyroxene + minor garnet (Figs. 6b and e). The magnetite grains in banded and massive iron ores are homogenous (Figs. 6h and i). (3) Massive iron ores, with magnetite as dominant mineral with minor amphibole, calcite, and epidote (Figs. 6c, f and 5 h). Magnetite is closely associated and in textural equilibrium with amphibole, epidote, and ilvaite (Figs. 7d, f, h and i).

Two distinct generations of magnetite, namely early magnetite (Mt_1) and late magnetite (Mt_2), have been recognized in the iron ores. In general, the late magnetite is darker than the early magnetite under BSE imaging (Fig. 12d). The early formed magnetite is in equilibrium with garnet whereas the late magnetite has weak oscillatory zoning.

4.3. Paragenesis

On the basis of field investigation and microscope observations, four paragenetic stages of mineralization have been recognized as follows: (I) pre-ore K-Na alteration, (II) skarn stage with minor disseminated iron mineralization, (III) retrograde skarn alteration associated with massive iron mineralization, and (IV) calcite-quartz-sulfide stage associated with minor cobalt mineralization (Fig. 8).

5. Samples and analytical techniques

5.1. Electron microprobe analysis

Mineral compositions were carried out using a JXA-8230 electron microprobe at the Chinese Academy of Geological Sciences,

Beijing. The ZAF correction method, consisting of atomic number correction (Z), absorption correction (A), and fluorescence correction (F), was used for standardization. The standards are the following: albite (Al, Na), rutile (Ti), hematite (Fe), MnO (Mn), MgO (Mg), potassium feldspar (K), nepheline (Si). The samples were analyzed with an accelerating voltage of 15 kV and a beam current of 20 nA. The regular minerals were analyzed with 5 μm beam diameter and the smaller minerals ($<10 \mu\text{m}$) were analyzed with 1 μm spot. Peak and background counting times were set at 10 and 5 s, respectively.

5.2. Fluid inclusions and microthermometric measurements

Thirty-seven garnet, pyroxene, epidote, quartz and calcite samples were selected from the skarn, retrograde altered skarn and quartz-sulfide -carbonate stage in the Cihai deposit. Fluid inclusions are widely present in skarn minerals, quartz, and calcite of the Cihai Fe deposit. Most of these inclusions are isolated, thought to be primary, and interpreted to represent the fluid from which garnet, pyroxene, epidote, quartz, and calcite formed during different stages. These inclusions have ellipsoidal, columnar, irregular shapes and range from 5 to 40 μm in size. The types of fluid inclusion and their characteristics are listed in Table 3 and shown in Fig. 13.

For prograde skarn stage, garnet has more abundant inclusions than clinopyroxene. Three types of primary fluid inclusions were recognized in garnet and clinopyroxene: hypersaline inclusions with halite (H; 10–40 vol% halite) at room temperature (Figs. 13a, b, e and g); liquid-rich two phase inclusions (L; 60–95 vol% liquid) with relatively small vapor bubbles and opaque

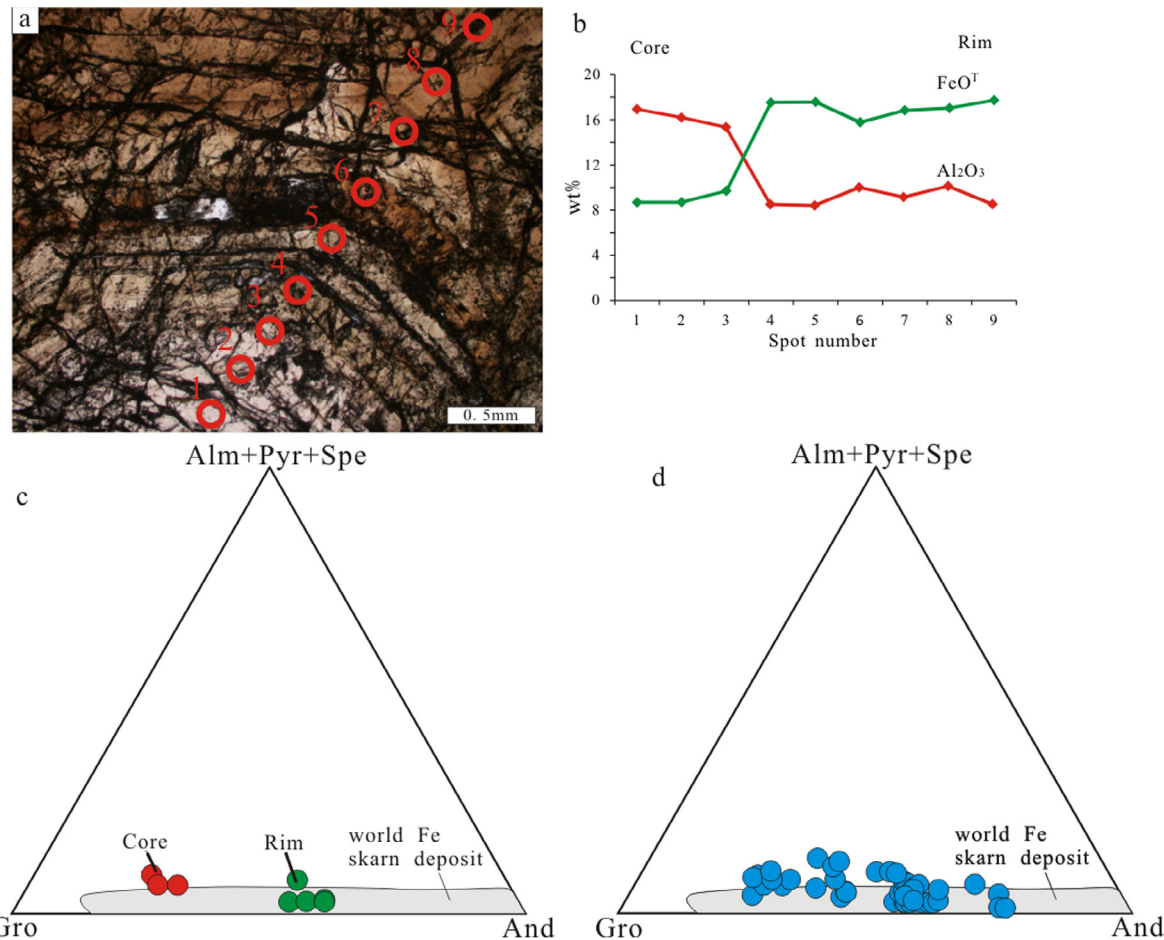


Fig. 9. Photomicrographs and compositions of garnet in the Cihai deposit. (a) Photomicrographs of garnet crystal with zoned texture, spot numbers are shown along the profile, plane-polarized light. (b) The variations in FeOT and Al_2O_3 of garnet grain along the profile. (c) End number composition of garnet crystal with zoned texture. (d) End number composition of all garnet crystals from Cihai iron deposit. The compositional fields for garnet in Fe skarn deposits (Meinert et al., 2005) are shown in diagram for comparison. Mineral abbreviations: And = andradite, Alm = almandine, Gro = grossular, Pyr = pyrope, Spe = spessartine.

minerals (Figs. 13f and h); and vapor-rich (V; >70 vol% vapor) inclusions (Figs. 13a, c and d). Epidote is an ideal host mineral for retrograde skarn stage inclusions, in which liquid-rich two phase inclusions are commonly present (Figs. 13i and j). For the quartz-calcite-sulfide stage, abundant liquid-rich two-phase inclusions are present in quartz and calcite (Figs. 13k and l).

The petrographic characteristics of fluid inclusions were studied, and their types and assemblages were distinguished by optical microscopy of doubly polished sections (~200–300 μm in thickness). The microthermometric measurements of fluid inclusions follow the procedure of Shepherd et al. (1985). Microthermometric analysis was undertaken using a LINKAM THMGS-600 programmable heating and freezing stage with a temperature range of $-196\text{ }^\circ\text{C}$ – $600\text{ }^\circ\text{C}$ at the China University of Geosciences, Beijing, China. The reproducibility of these measurements is $\pm 0.1\text{ }^\circ\text{C}$ below $30\text{ }^\circ\text{C}$, and heating and freezing temperatures were reproducible within $\pm 1\text{ }^\circ\text{C}$ and $\pm 0.1\text{ }^\circ\text{C}$, respectively. Salinities of all inclusions are reported as wt.% NaCl equiv (Table 3; Fig. 14).

5.3. Oxygen and hydrogen isotopes

A total of seventeen garnet and quartz samples were used for oxygen and hydrogen isotope analysis. Six magnetite samples were used for oxygen isotope analysis. Mineral separation was carried out at the Langfang Geochemical Laboratory in Hebei Province,

China. All mineral separates were examined using a binocular microscope prior to isotope analysis to ensure 99% purity.

Isotope analyses were performed using a MAT-253 EM spectrometer at the Isotopic Laboratory of the Institute of Mineral Resources, Chinese Academy of Geological Sciences (CAGS), Beijing, China. The analytical uncertainty was $\pm 0.2\text{\textperthousand}$ for oxygen and $\pm 2\text{\textperthousand}$ for hydrogen isotope analysis. Oxygen isotopic analysis was undertaken using the BrF_5 method (Clayton and Mayeda, 1963), where 12 mg of pure quartz is reacted with BrF_5 for 15 h to produce oxygen, before this oxygen is transferred to a CO_2 transformation system at a temperature of $700\text{ }^\circ\text{C}$ for CO_2 collection after 12 min, as outlined in Mao et al. (2002). Hydrogen isotope analysis involved the release of water from fluid inclusions by crushing; this water was then reacted with zinc for 30 min at temperature of $400\text{ }^\circ\text{C}$ to produce hydrogen (Coleman et al., 1982), which was transferred to a sample bottle filled with activated carbon after freezing in liquid nitrogen.

For the oxygen isotope analyses we used an approach where calcite was reacted with phosphoric acid to release CO_2 at $25\text{ }^\circ\text{C}$ (McCrea, 1950). Chinese high-quality carbonate reference materials for oxygen (GBW04416 and GBW04417) were used as a working standard, and the $\delta^{18}\text{O}_{\text{PDB}}$ (Peedee Belemnite, PDB) values of GBW04416 and GBW04417 were $-11.59\text{\textperthousand}$ and $-24.12\text{\textperthousand}$, respectively. The $\delta^{18}\text{O}_{\text{PDB}}$ value of calcite was directly measured from the CO_2 obtained during the reaction between calcite and phosphoric acid. The $\delta^{18}\text{O}$ are reported with respect to Standard Mean Ocean

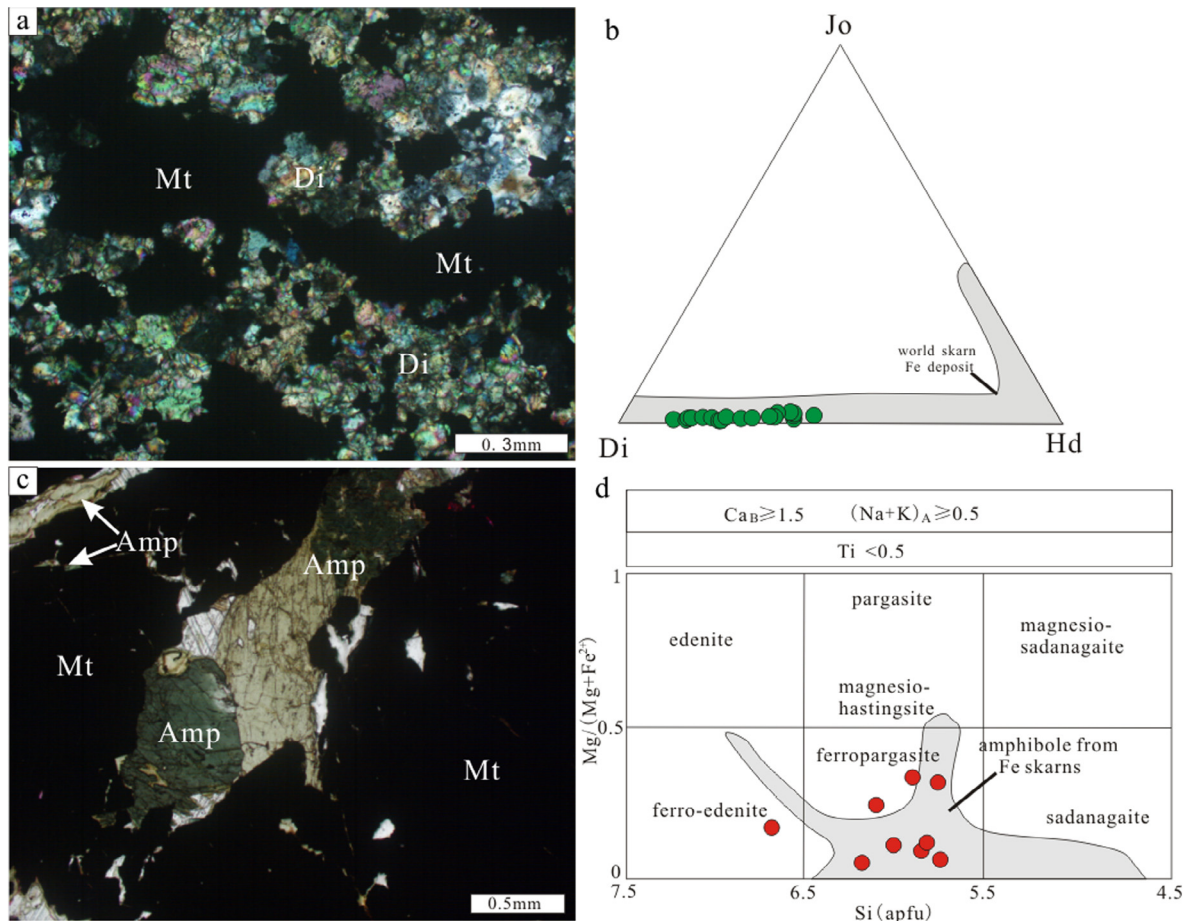


Fig. 10. (a) Photomicrographs of clinopyroxene crystal associated with iron mineralization, crossed-polarized light. (b) End number composition of all clinopyroxene crystals associate with iron mineralization from Cihai iron deposit. The compositional fields for clinopyroxene in Fe skarn deposits (Meinert et al., 2005) are shown in diagram for comparison. (c) Photomicrographs of amphibole intergrowth with massive magnetite, plane-polarized light. (d) Composition of amphibole from the Cihai retrograde alteration stages associated with massive magnetite. The compositional fields for amphibole in Fe skarn deposits (Pons et al., 2009) are shown in diagram for comparison.

Water (SMOW). The $\delta^{18}\text{O}_{\text{SMOW}} = 1.03086 * \delta^{18}\text{O}_{\text{PDB}} + 30.86$ (Friedman and O'Neil, 1977) equation was used to determine $\delta^{18}\text{O}_{\text{SMOW}}$ values from $\delta^{18}\text{O}_{\text{PDB}}$.

6. Results

6.1. EMPA results

Results of EPMA for garnet, clinopyroxene, and amphibole in the Cihai deposit are listed in [Supplemental Table 1–3](#), respectively. Microprobe analyses of garnet crystals show a wide compositional range (And_{9–74}Gro_{24–85}; [Fig. 9d](#)) as well as zonation of individual crystals from cores of grossularite composition (And_{23–29}Gro_{65–69}) to more andraditic rims (And_{52–60}Gro_{38–45}) ([Figs. 9b and c](#)). Microprobe analyses of iron mineralization associated clinopyroxene crystals indicate that they belong to diopside, and show a wide compositional range (Hd_{16–56}Di_{44–83}Jo_{0–3}; [Fig. 10b](#)). Overall, most garnet and clinopyroxene in the Cihai Fe deposit display compositions similar to those from other skarn Fe deposits ([Figs. 9d and 10b](#); Meinert et al., 2005). The results of microprobe analyses indicate that amphibole are iron rich, and most of them belong to ferropargasite ([Fig. 10d](#); [Supplemental Table 3](#)). Amphibole grains in the Cihai Fe deposit also show compositions similar to those from other skarn Fe deposits ([Fig. 10d](#); Pons et al., 2009).

Results of EPMA for magnetite in disseminated, banded, and massive magnetite ores are presented in [Table 1](#). Generally, TiO₂ contents of magnetite from the disseminated ores (n = 25; 0–1.75 wt.%, mean = 0.56 wt.%), banded ores (n = 15; 0–0.79 wt.%, mean = 0.28 wt.%), and massive ores (n = 24; 0–0.34 wt.%, mean = 0.09 wt.%) generally decrease ([Figs. 11a and c](#)). In contrast, MgO contents of magnetite from the disseminated ores (n = 25; 0–0.37 wt.%, mean = 0.08 wt.%), banded ores (n = 15; 0–0.43 wt.%, mean = 0.10 wt.%), and massive ores (n = 24; 0–1.25 wt.%, mean = 0.15 wt.%) gradually increase. In the Ca + Al + Mn versus Ti + V diagram, magnetite from the disseminated, banded, and massive ores at Cihai are plotted in or close to the skarn field ([Fig. 11b](#)), consistent with its crystallization from hydrothermal fluids. Similarly, all three type ores have very low concentration of V₂O₃, with average concentration V₂O₃ = 0.02 wt.%, 0.02 wt.% and 0.01 wt.%, respectively ([Fig. 11c](#)).

Results of EPMA for a representative single magnetite grain with two distinct generations including early-formed magnetite (Mt₁) and late magnetite (Mt₂) in the banded ores are presented in [Table 2](#). The early-formed magnetite (Mt₁) has much higher FeO^T (91.75–93.38 wt.%), TiO₂ (0.20–0.49 wt.%), and Al₂O₃ (0.45–1.89 wt.%) contents than FeO^T (86.77–88.36 wt.%), TiO₂ (0.02–0.07 wt.%), and Al₂O₃ (0.56–0.90 wt.%) contents of the late magnetite (Mt₂). However, the Mt₁ has lower CaO and SiO₂ con-

Table 1

EMPA data for magnetite in disseminated, banded, and massive iron ores from the Cihai iron deposit.

No.	Sample	SiO ₂	TiO ₂	Al ₂ O ₃	Cr ₂ O ₃	FeO ^T	MnO	NiO	MgO	CaO	Na ₂ O	K ₂ O	P ₂ O ₅	V ₂ O ₃	Total
<i>Disseminated iron ores</i>															
1	CH12-05-2-1	0.02	0.36	1.60	0.00	89.81	0.30	0.00	0.06	0.00	0.00	0.01	0.00	0.04	92.21
2	CH12-49-1-1-1	0.07	0.39	0.71	0.02	92.30	0.03	0.04	0.06	0.00	0.02	0.00	0.00	0.00	93.65
3	CH12-49-1-2-2	0.05	0.80	1.37	0.08	91.11	0.13	0.00	0.04	0.00	0.00	0.00	0.00	0.11	93.68
4	CH12-50-1-3-3	0.03	0.09	0.86	0.03	91.28	0.16	0.03	0.02	0.00	0.00	0.00	0.02	0.00	92.51
5	CH12-50-1-4-1	0.64	0.17	0.88	0.06	90.35	0.13	0.01	0.33	0.00	0.05	0.01	0.00	0.00	92.62
6	CH12-102-1-3	0.09	1.75	1.28	0.03	90.62	0.28	0.00	0.03	0.01	0.14	0.01	0.00	0.01	94.24
7	CH12-102-2-4	0.01	1.33	0.99	0.05	91.80	0.17	0.00	0.06	0.01	0.05	0.00	0.01	0.04	94.53
8	CH12-117-1-3	0.06	0.82	0.97	0.01	91.89	0.16	0.01	0.03	0.00	0.02	0.00	0.01	0.03	94.00
9	CH12-117-2-3	0.10	0.20	0.21	0.06	92.15	0.03	0.01	0.00	0.00	0.09	0.02	0.00	0.03	92.90
10	CH12-117-3-3	0.69	0.20	1.07	0.02	90.65	0.02	0.00	0.17	0.00	0.07	0.01	0.00	0.00	92.88
11	CH12-135-1-3	0.09	0.16	0.56	0.00	93.12	0.25	0.09	0.02	0.00	0.04	0.00	0.00	0.01	94.35
12	CH12-135-2-3	0.73	0.80	1.29	0.06	89.42	0.47	0.00	0.37	0.00	0.20	0.00	0.02	0.02	93.37
13	CH12-135-3-1	0.07	0.04	1.60	0.00	91.38	0.51	0.01	0.21	0.00	0.13	0.00	0.02	0.01	93.98
14	CH12-135-3-2	0.05	0.16	1.04	0.00	91.40	0.50	0.02	0.09	0.00	0.38	0.02	0.00	0.00	93.66
15	CN12-2-1-1	0.23	0.69	1.63	0.07	89.56	0.01	0.00	0.05	0.03	0.05	0.00	0.00	0.10	92.42
16	CN12-02-3-2-1	0.07	0.68	5.03	0.06	88.27	0.16	0.00	0.07	0.00	0.00	0.00	0.00	0.04	94.40
17	CN12-08-3-1	0.12	1.37	2.09	0.07	89.25	0.12	0.00	0.02	0.00	0.00	0.01	0.00	0.07	93.10
18	CN12-09-1-1	0.04	0.34	2.09	0.07	90.55	0.64	0.00	0.07	0.00	0.03	0.00	0.01	0.02	93.86
19	CN12-09-2-1	0.03	1.06	2.95	0.03	89.33	0.58	0.00	0.10	0.00	0.05	0.00	0.00	0.02	94.14
20	CN12-64-1-2	0.09	0.30	0.78	0.11	90.60	0.16	0.01	0.00	0.00	0.02	0.00	0.01	0.00	92.09
21	CN12-64-2-2	0.12	0.53	0.93	0.10	90.84	0.13	0.00	0.00	0.08	0.01	0.00	0.00	0.00	92.74
22	CN12-64-3-3	0.11	1.00	2.18	0.15	89.65	0.20	0.00	0.04	0.00	0.07	0.00	0.01	0.00	93.40
23	CN12-84-1-3	0.10	0.00	0.46	0.02	92.67	0.05	0.03	0.04	0.03	0.08	0.01	0.06	0.01	93.54
24	CN12-84-2-2	0.06	0.58	3.02	0.00	89.48	0.29	0.00	0.05	0.05	0.08	0.01	0.00	0.00	93.63
25	CN12-84-3-3	0.14	0.09	0.19	0.04	90.98	0.10	0.00	0.01	0.06	0.31	0.01	0.01	0.00	91.94
<i>Banded iron ores</i>															
1	CX12-43-1-3	1.16	0.16	1.41	0.00	90.30	0.21	0.01	0.33	0.16	0.02	0.00	0.00	0.05	93.80
2	CX12-43-2-2	0.05	0.39	1.39	0.00	91.79	0.14	0.00	0.00	0.11	0.00	0.00	0.03	0.04	93.94
3	CX12-43-2-3	4.08	0.00	0.57	0.03	88.88	0.08	0.00	0.05	0.70	0.12	0.05	0.00	0.04	94.61
4	CX12-43-2-4	0.06	0.43	1.48	0.00	92.26	0.21	0.00	0.08	0.00	0.15	0.02	0.00	0.04	94.72
5	CX12-43-3-2	0.08	0.27	1.85	0.00	90.77	0.34	0.00	0.27	0.00	0.01	0.00	0.00	0.04	93.63
6	CX12-44-1-3	0.07	0.30	1.28	0.01	92.69	0.16	0.00	0.00	0.00	0.02	0.00	0.01	0.02	94.55
7	CX12-44-1-4	0.08	0.31	1.51	0.00	91.57	0.16	0.03	0.05	0.00	0.06	0.01	0.00	0.00	93.77
8	CX12-44-2-2	0.06	0.46	1.39	0.01	91.58	0.16	0.00	0.06	0.05	0.05	0.00	0.00	0.02	93.84
9	CX12-44-2-3	0.20	0.28	2.23	0.01	89.08	0.22	0.02	0.43	0.04	0.00	0.00	0.00	0.00	92.50
10	CX12-44-3-2	0.09	0.23	1.41	0.00	90.73	0.18	0.00	0.03	0.02	0.06	0.01	0.01	0.00	92.77
11	CX12-44-3-3	0.05	0.12	1.04	0.00	91.85	0.18	0.00	0.09	0.00	0.02	0.01	0.01	0.00	93.37
12	CX12-44-3-4	0.13	0.16	0.31	0.00	92.71	0.11	0.00	0.00	0.00	0.06	0.01	0.01	0.01	93.51
13	CX12-21-1-2	0.25	0.08	1.02	0.00	91.67	0.13	0.00	0.03	0.00	0.21	0.01	0.04	0.04	93.48
14	CX12-21-3-2	0.11	0.79	1.76	0.04	88.54	0.39	0.05	0.01	0.41	0.21	0.02	0.04	0.05	92.39
15	CX12-21-3-3	0.42	0.19	1.13	0.00	92.37	0.14	0.00	0.04	0.00	0.15	0.00	0.00	0.01	94.45
<i>Massive iron ores</i>															
1	CH12-25-1-1	0.03	0.09	0.82	0.00	91.59	0.43	0.02	0.10	0.00	0.04	0.01	0.01	0.00	93.13
2	CH12-25-2-2	0.02	0.00	0.72	0.00	93.10	0.31	0.00	0.05	0.00	0.05	0.01	0.00	0.00	94.28
3	CH12-25-3-1	0.06	0.04	0.86	0.03	92.27	0.34	0.00	0.05	0.00	0.00	0.01	0.00	0.00	93.66
4	CH12-25-3-2	0.08	0.03	0.78	0.05	92.88	0.18	0.00	0.02	0.00	0.03	0.02	0.00	0.00	94.07
5	CH12-25-4-1	0.00	0.12	0.90	0.03	93.44	0.07	0.02	0.02	0.00	0.00	0.01	0.00	0.00	94.60
6	CH12-84-1-2	0.11	0.34	2.19	0.01	91.98	0.28	0.01	0.02	0.00	0.07	0.00	0.00	0.06	95.06
7	CH12-84-2-1	0.17	0.07	2.27	0.04	91.44	0.32	0.03	0.14	0.00	0.18	0.01	0.00	0.00	94.66
8	CH12-84-3-1	0.22	0.03	2.41	0.00	89.55	0.32	0.04	0.13	0.00	0.15	0.01	0.00	0.04	92.90
9	CH12-139-2-1	0.23	0.08	1.73	0.00	90.71	0.11	0.00	0.14	0.00	0.07	0.02	0.00	0.02	93.12
10	CH12-139-3-1	0.28	0.16	0.95	0.01	90.67	0.17	0.00	0.05	0.00	0.04	0.00	0.01	0.00	92.34
11	CH12-139-4-3	0.16	0.15	1.77	0.00	91.42	0.11	0.02	0.12	0.03	0.00	0.00	0.00	0.00	93.77
12	CH12-144-1-1	0.13	0.00	0.95	0.00	91.48	0.32	0.01	0.12	0.00	0.04	0.02	0.02	0.00	93.08
13	CH12-144-2-2	0.06	0.13	0.91	0.01	91.68	0.08	0.03	0.00	0.00	0.00	0.00	0.00	0.02	92.93
14	CH12-144-3-2	0.11	0.03	0.62	0.03	92.25	0.09	0.00	0.01	0.00	0.05	0.00	0.00	0.01	93.21
15	CH12-171-1-2	0.20	0.04	0.89	0.00	91.77	0.19	0.00	0.04	0.00	0.13	0.02	0.05	0.00	93.33
16	CH12-171-4-1	0.34	0.12	1.04	0.04	91.65	0.15	0.00	0.11	0.00	0.12	0.00	0.03	0.01	93.61
17	CH12-171-2-1	0.08	0.00	1.24	0.00	91.98	0.09	0.00	0.07	0.00	0.00	0.00	0.00	0.00	93.46
18	CH12-171-2-2	0.26	0.00	0.95	0.01	91.02	0.14	0.00	0.02	0.00	0.04	0.00	0.01	0.00	92.45
19	CH12-171-3-1	1.34	0.22	5.67	0.02	84.87	0.12	0.00	1.25	0.68	0.20	0.00	0.00	0.02	94.38
20	CN12-05-1-1	0.05	0.18	2.10	0.00	89.65	0.15	0.04	0.18	0.00	0.12	0.03	0.00	0.01	92.49
21	CN12-05-2-2	0.11	0.11	2.12	0.04	89.69	0.03	0.00	0.15	0.00	0.03	0.00	0.00	0.00	92.29
22	CN12-86-1-2	1.50	0.00	0.01	0.03	89.27	0.12	0.04	0.65	0.24	0.00	0.00	0.00	0.00	91.84
23	CN12-86-1-4	0.07	0.00	2.26	0.00	92.18	0.07	0.00	0.12	0.00	0.02	0.00	0.00	0.00	94.71
24	CN12-86-2-4	0.11	0.10	2.86	0.01	89.99	0.06	0.00	0.05	0.00	0.08	0.00	0.03	0.00	93.27

tents than Mt₂, with 0.12–0.34 wt.% CaO and 0.04–0.11 wt.% SiO₂ compared to 0.87–1.89 wt.% CaO and 3.59–5.24 wt.% SiO₂ (Fig. 12). The Ti + V vs. Al + Mn plot for Mt₁ and Mt₂ (Fig. 12i) shows a decreasing temperature trend as suggested by Nadoll et al. (2014).

6.2. Microthermometric results

A total of 262 fluid inclusions from 37 samples from the prograde skarn stage, retrograde skarn stage, and quartz- calcite-sulfide stage were analyzed, and the results are summarized in in

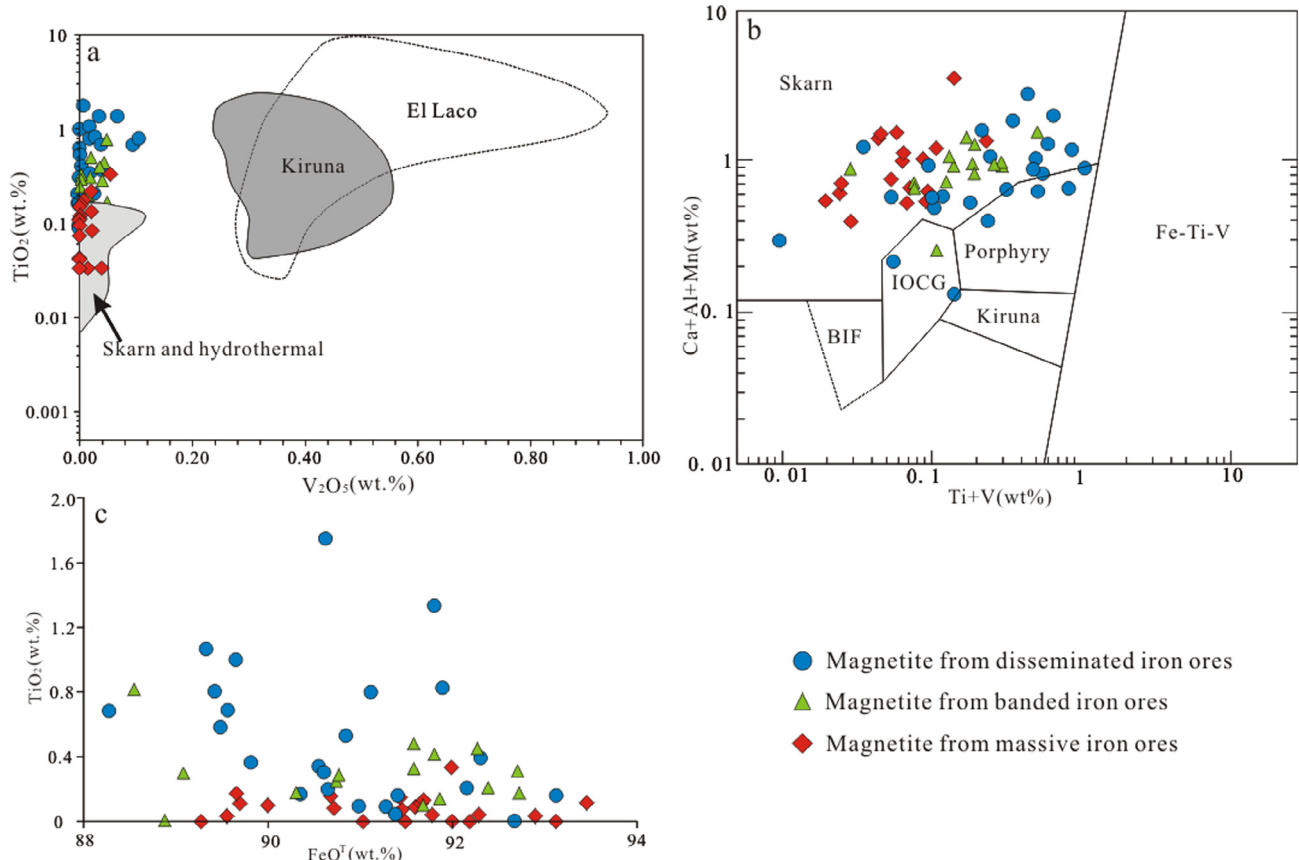


Fig. 11. Compositional variations of magnetite from disseminated, banded and massive iron ores in the Cihai deposit. (a) Plot of V_2O_5 vs. TiO_2 (wt.%) of magnetite from the disseminated, banded, and massive iron ores. The reference area is from Hou et al. (2011); (b) Plot of $\text{Ti} + \text{V}$ vs. $\text{Ca} + \text{Al} + \text{Mn}$ (wt.%) of magnetite from the disseminated, banded, and massive iron ores. The reference fields are from Dupuis and Beaudoin (2011); (c) FeOT vs. TiO_2 plot showing that magnetite from the disseminated iron ores has geochemical characteristics significantly different from the banded and massive iron ores.

Table 2
EMPA data for zoned magnetite grain from Cihai iron deposit.

No.	Sample	SiO_2	TiO_2	Al_2O_3	Cr_2O_3	FeOT	MnO	NiO	MgO	CaO	Na_2O	K_2O	V_2O_3	Total
1	CX12-43-2-3 Line 001	3.59	0.07	0.56	0.00	87.09	0.13	0.11	0.07	1.89	0.13	0.04	0.01	93.68
2	CX12-43-2-3 Line 002	4.72	0.03	0.72	0.00	88.34	0.14	0.01	0.05	1.11	0.21	0.08	0.05	95.46
3	CX12-43-2-3 Line 003	5.24	0.02	0.90	0.00	88.36	0.14	0.01	0.08	0.87	0.19	0.11	0.05	95.96
4	CX12-43-2-3 Line 004	0.11	0.20	0.45	0.07	93.21	0.09	0.02	0.00	0.16	0.00	0.01	0.12	94.42
5	CX12-43-2-3 Line 005	0.04	0.39	1.10	0.04	92.34	0.12	0.00	0.01	0.12	0.05	0.00	0.00	94.22
6	CX12-43-2-3 Line 006	0.09	0.49	1.89	0.00	91.75	0.07	0.00	0.02	0.15	0.00	0.01	0.01	94.48
7	CX12-43-2-3 Line 007	0.09	0.37	1.36	0.00	92.17	0.09	0.00	0.01	0.14	0.02	0.00	0.01	94.26
8	CX12-43-2-3 Line 008	0.10	0.30	1.39	0.00	92.66	0.07	0.00	0.00	0.22	0.03	0.00	0.00	94.77
9	CX12-43-2-3 Line 009	0.08	0.38	0.89	0.04	93.38	0.11	0.00	0.00	0.34	0.06	0.00	0.06	95.34
10	CX12-43-2-3 Line 010	4.42	0.03	0.68	0.02	86.77	0.15	0.00	0.09	1.41	0.16	0.08	0.00	93.81

Table 3 and shown in Fig. 14. Salinities of L- and V-type fluid inclusions were calculated using the equation for the $\text{NaCl}-\text{H}_2\text{O}$ system given by Bodnar (1993).

A total of 102 fluid inclusions were analyzed from garnet and clinopyroxene from the prograde skarn stage. Heating measurement yielded final homogenization temperatures between 271° and 600 °C, most of which were between 520° and 600 °C (Fig. 14a). Ice-melting temperatures from the two-phase aqueous inclusions range from -21.0° to -5.2 °C, corresponding to moderate salinities from 8.1 to 23.1 wt.% NaCl equiv. Halite dissolution temperatures varying from 388° to 569 °C, corresponding to salinities from 46.2 to 69.5 wt.% NaCl equiv (Fig. 14d).

Forty-eight fluid inclusions within epidote from the retrograde skarn stage were analyzed. Heating measurement yielded final homogenization temperatures between 160° and 456 °C, most of which were between 220° and 456 °C (Fig. 14b). Ice-melting tem-

peratures from the two-phase aqueous inclusions range from -12.4° to -5.4 °C, corresponding to moderate salinities from 8.4 to 16.3 wt.% NaCl equiv (Fig. 14e).

In the calcite-quartz-sulfide stage, a total of 112 fluid inclusions, of which 63 were from quartz and 49 were from calcite, were analyzed. Heating measurement yielded final homogenization temperatures between 128° and 367 °C, most of which were between 140° and 340 °C (Fig. 14c). Ice-melting temperatures from the two-phase aqueous inclusions range from -20.7° to -0.1 °C, corresponding to moderate salinities from 0.2 to 22.9 wt.% NaCl equiv (Fig. 14f).

6.3. Pressure estimation

Selected microthermometric determination of fluid inclusions can provide information on pressure conditions (Hedenquist

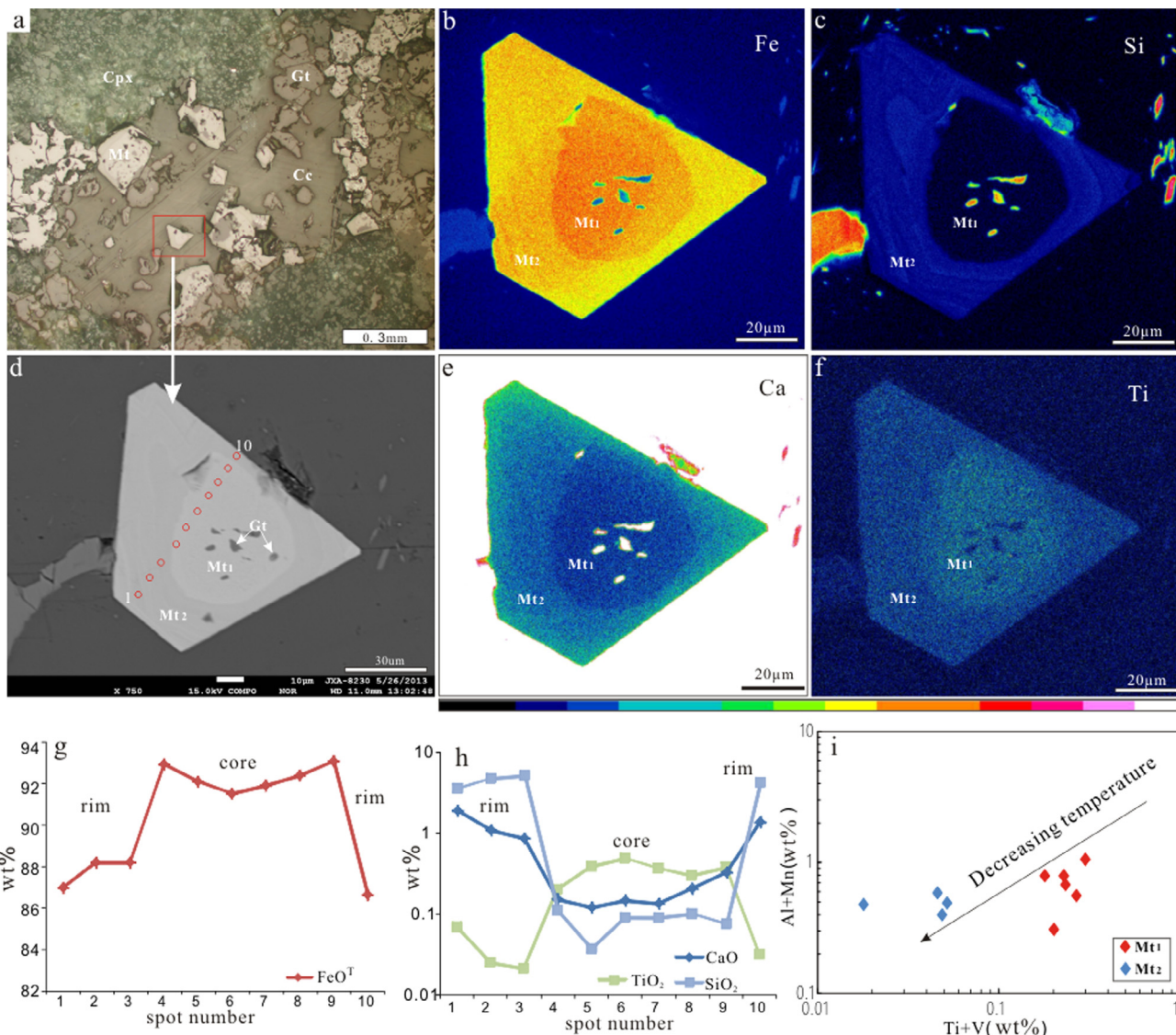


Fig. 12. Compositional transects of representative magnetite sample from the Cihai banded ores. (a) Euhedral-subhedral magnetite grains in the banded ores, reflected-light; (b–f) Compositional zoning of a magnetite including early stage magnetite (Mt₁) and late stage magnetite (Mt₂); (g and h) Variations in FeO^T, TiO₂, CaO and SiO₂ of the magnetite grain along the profile; (i) The Ti + V vs. Al + Mn plot for Mt₁ and Mt₂ show a decreasing temperature trend (after Nadoll et al. 2014). Mineral abbreviations: Cpx = clinopyroxene, Mt = magnetite, Cc = calcite, Gt = garnet.

et al., 1998). Boiling assemblages will give exact fluid entrapment temperatures (Roedder and Bodnar, 1980), which can be estimated for trapping pressure. By contrast, pressures determined for non-boiling assemblages are derived from the homogenization temperature and represent minimum values (Rusk et al., 2008).

As described above, evidence for boiling in a prograde skarn assemblage suggesting that homogenization temperatures can be interpreted to closely approximate trapping temperatures, thus trapping pressures can also be estimated. Lack of evidence for boiling in the retrograde skarn silicate minerals only permits the estimation of minimum trapping temperatures and pressures for the late fluids. Estimated trapping pressures from fluid inclusions can be obtained by fluid data in the binary system NaCl–H₂O in the prograde skarn ore stage (Fig. 15; Driesner and Heinrich, 2007). As shown in Fig. 15, the average estimated trapping pressures for fluid inclusions near the critical curve of the prograde skarn stage are at ~700 bars, corresponding to ~2 km under lithostatic conditions. The estimated trapping pressures for H-type fluid inclusions of the prograde skarn stage are concentrated at ~500 bars. Liquid

rich type fluid inclusions occur within retrograde skarn stage minerals are also displayed in Fig. 15 and their trapping pressures are concentrated at ~100 bars, representing their minimum trapping pressures at ~1 km under hydrostatic conditions.

6.4. Stable isotope geochemistry

The oxygen and hydrogen isotope compositions of samples from the prograde skarn and quartz-sulfide stage in the Cihai Fe deposit are listed in Table 4 and plotted in Fig. 16. The $\delta_{\text{Dv-SMOW}}$ values of 5 garnet samples vary widely from $-116\text{\textperthousand}$ to $-76\text{\textperthousand}$, although the $\delta^{18}\text{O}_{\text{v-SMOW}}$ values fall in a relatively narrow range from $6.3\text{\textperthousand}$ to $10.6\text{\textperthousand}$. Using the fractionation factors of Bottinga and Javoy (1975) for garnet and the average homogenization temperature of fluids inclusions of the same sample, the $\delta^{18}\text{O}_{\text{fluid}}$ values of the mineralizing fluids are calculated to be $4.5\text{\textperthousand}$ – $8.7\text{\textperthousand}$. The $\delta_{\text{Dv-SMOW}}$ values of 12 quartz samples vary widely from $-116\text{\textperthousand}$ to $-78\text{\textperthousand}$, by contrast, the $\delta^{18}\text{O}_{\text{v-SMOW}}$ values fall in a relatively narrow range from $9.0\text{\textperthousand}$ to $14.4\text{\textperthousand}$. Using the quartz–water

Table 3

Fluid inclusion data from the Cihai deposit.

Sample	Stage	Mineral	Phase composition	Th (L + V) (°C)	Tm _{ice} (°C)	Salinity (wt.% NaCl eq.)
CH12-95	Prograde skarn(II)	Pyroxene	L + V, V	311–526	−6.8/−5.2	8.14–10.24
CH12-95	Prograde skarn(II)	Garnet	L + V	463–600		
CH12-96	Prograde skarn(II)	Pyroxene	L + V	485–563		
CH12-96	Prograde skarn(II)	Garnet	L + V, H, V	377–597		46.16–69.49
CH12-118	Prograde skarn(II)	Garnet	L + V	556–600		
CH12-118	Prograde skarn(II)	Pyroxene	L + V	454–600		
CH12-123	Prograde skarn(II)	Garnet	L + V	412–598		
CH12-123	Prograde skarn(II)	Pyroxene	L + V,	543–596		
CN12-55	Prograde skarn(II)	Garnet	L + V,	271–599	−6.7	10.11
CN12-60	Prograde skarn(II)	Garnet	L + V	454–586		
CX12-39	Prograde skarn(II)	Garnet	L + V	384–596	−21.0/−20.5	22.71–23.05
CX12-40	Prograde skarn(II)	Garnet	L + V, H, V	569–599		59.90–61.13
CX12-41	Prograde skarn(II)	Garnet	L + V, H, V	341–594	−20.0/−10.8	8.41–63.77
CX12-52	Prograde skarn(II)	Garnet	L + V	342–597	−8.2	11.93
CX12-52	Prograde skarn(II)	Pyroxene	L + V	422–598	−20.8/−10.2	14.15–22.91
CN12-41	Retrograde skarn(III)	Epidote	L + V	229–409	−11.0/−8.7	12.51–14.97
CN12-42	Retrograde skarn(III)	Epidote	L + V	272–456	−12.4/−8.9	12.73–16.34
CN12-63	Retrograde skarn(III)	Epidote	L + V	160–343	−9.4/−5.4	8.41–13.29
CH-81	Quartz-sulfide-calcite(IV)	Quartz	L + V	194–367	−13.8/−5.8	8.95–17.61
CH-82	Quartz-sulfide-calcite(IV)	Quartz	L + V	147–197	−13.8/−1.1	1.91–17.61
CH-83	Quartz-sulfide-calcite(IV)	Quartz	L + V	158–207	−10.1/−0.5	0.88–14.04
CH-119	Quartz-sulfide-calcite(IV)	Quartz	L + V	138–320	−6.5/−0.1	0.18–9.86
CH-161	Quartz-sulfide-calcite(IV)	Quartz	L + V	190–360	−6.0/−1.0	1.74–9.21
CH-164	Quartz-sulfide-calcite(IV)	Quartz	L + V	230–299	−20.7/−6.0	9.21–22.85
CH-165	Quartz-sulfide-calcite(IV)	Quartz	L + V	282–332	−20.1/−16.3	19.68–22.44
CN12-49	Quartz-sulfide-calcite(IV)	Quartz	L + V	192–300	−9.4/−7.5	11.10–13.29
CN12-67	Quartz-sulfide-calcite(IV)	Quartz	L + V	171–198	−18.5/−12.1	16.05–21.33
CN12-68	Quartz-sulfide-calcite(IV)	Quartz	L + V	176–192	−15.2/−12.5	16.43–18.80
CX12-31	Quartz-sulfide-calcite(IV)	Quartz	L + V	246–338	−11.0/−6.2	9.47–14.97
CX12-32	Quartz-sulfide-calcite(IV)	Quartz	L + V	211–347	−10.4/−5.3	8.28–14.36
CH12-45	Quartz-sulfide-calcite(IV)	Calcite	L + V	142–350	−10.0/−2.0	3.39–13.94
CH12-46	Quartz-sulfide-calcite(IV)	Calcite	L + V	140–320	−12.0/−2.0	3.39–15.96
CH12-104	Quartz-sulfide-calcite(IV)	Calcite	L + V	145–193	−14.8/−8.7	12.51–18.47
CH12-122	Quartz-sulfide-calcite(IV)	Calcite	L + V	142–167	−11.8/−3.1	5.11–15.76
CX12-27	Quartz-sulfide-calcite(IV)	Calcite	L + V	147–187	−5.2/−2.7	4.49–8.14
CX12-28	Quartz-sulfide-calcite(IV)	Calcite	L + V	149–259	−5.9/−3.7	6.01–9.08
CN12-47	Quartz-sulfide-calcite(IV)	Calcite	L + V	128–258	−3.9/−0.2	0.35–6.30

Fluid inclusion type: H = hypersaline, L + V = liquid rich, V = vapor rich

fractionation equation of $1000\ln\alpha = 3.38 \times 10^6 T^{-2} - 3.40$ (Clayton et al., 1972) and the average homogenization temperature of fluids inclusions of the same sample, the $\delta^{18}\text{O}_{\text{fluid}}$ values of the mineralizing fluids are calculated to be $-3.7\text{\textperthousand}$ – $6.5\text{\textperthousand}$.

The oxygen isotope compositions of magnetite separated from the iron ores in the Cihai Fe deposit are listed in Table 5. The disseminated and massive iron ores from the main ore body yield $\delta^{18}\text{O}$ values, between +4.1 and +8.5‰ [n = 6] (Fig. 17).

7. Discussion

7.1. Genetic type of the Cihai deposit

The Cihai iron skarn deposit contains some features that have brought about different interpretations of its formation. Firstly, both the iron ores and the associated garnet-clinopyroxene skarn mineral assemblage are hosted in diabase, as opposed to carbonate sedimentary rock. Secondly, some of the magnetites within the deposit have relatively high TiO_2 content (Wang et al., 2006), which has been interpreted as of magmatic origin.

Two different models have been proposed to explain these features. One hypothesis invokes direct crystallization of immiscible Fe-rich melt that separated from a parent silicate magma, and with a later hydrothermal event overprints the former (Sheng, 1985; Zhao, 2000; Wang et al., 2006; Tang et al., 2010). The other hypothesis invokes deposition of magnetite from hydrothermal fluids only (Xue et al., 2000; Hou et al., 2013; Huang et al., 2013). The controversy focuses on whether there is a Fe-rich melt involved in the

formation of the Fe mineralization. According to previous studies, the main evidence of a Fe-rich melt during mineralization are: (1) some magnetite grains have high TiO_2 contents (TiO_2 0.086–1.558 wt.%, Wang et al., 2006) which were explained to be iron ores crystallized from a Fe-rich melt, (2) some massive iron ore bodies have sharp contact with host diabase and very weak or without alteration halos (Sheng, 1985; Zhao, 2000).

As the most dominant mineral in iron ores, magnetite can form in various environments including magmatic and hydrothermal, and usually has distinct concentrations of trace elements such as Ti, V, Si, Al, Mg, Cr, Mn, and Ca (Newberry et al., 1982; Westendorp et al., 1991; Shimazaki, 1998; Ryabchikov and Kogarko, 2006; Huberty et al., 2012; Nadoll et al., 2012; Hu et al., 2014). Thus, the compositions of magnetite can be used as a genetic indicator of different ore deposit types including Fe-Ti-V, Kiruna, BIF (banded iron formation), and skarn deposit (Dupuis and Beaudoin, 2011; Dare et al., 2014; Nadoll et al., 2014; Knipping et al., 2015a).

The disseminated, banded, and massive iron ores of the Cihai deposit represent gradual enrichment of iron (Fig. 6). As described above, the most distinctive feature of magnetite composition from these different ores is the TiO_2 content which generally decreases from disseminated, banded, and massive iron ores (Figs. 11a and c). The occurrence of relative high TiO_2 content magnetite grains from the Cihai deposit were considered as the evidence of Fe-rich melts (Wang et al., 2006). However, our study shows that the relatively high TiO_2 content of magnetite is only present in disseminated form in the prograde skarns, which are the alteration products of diabase. Our new data show that these

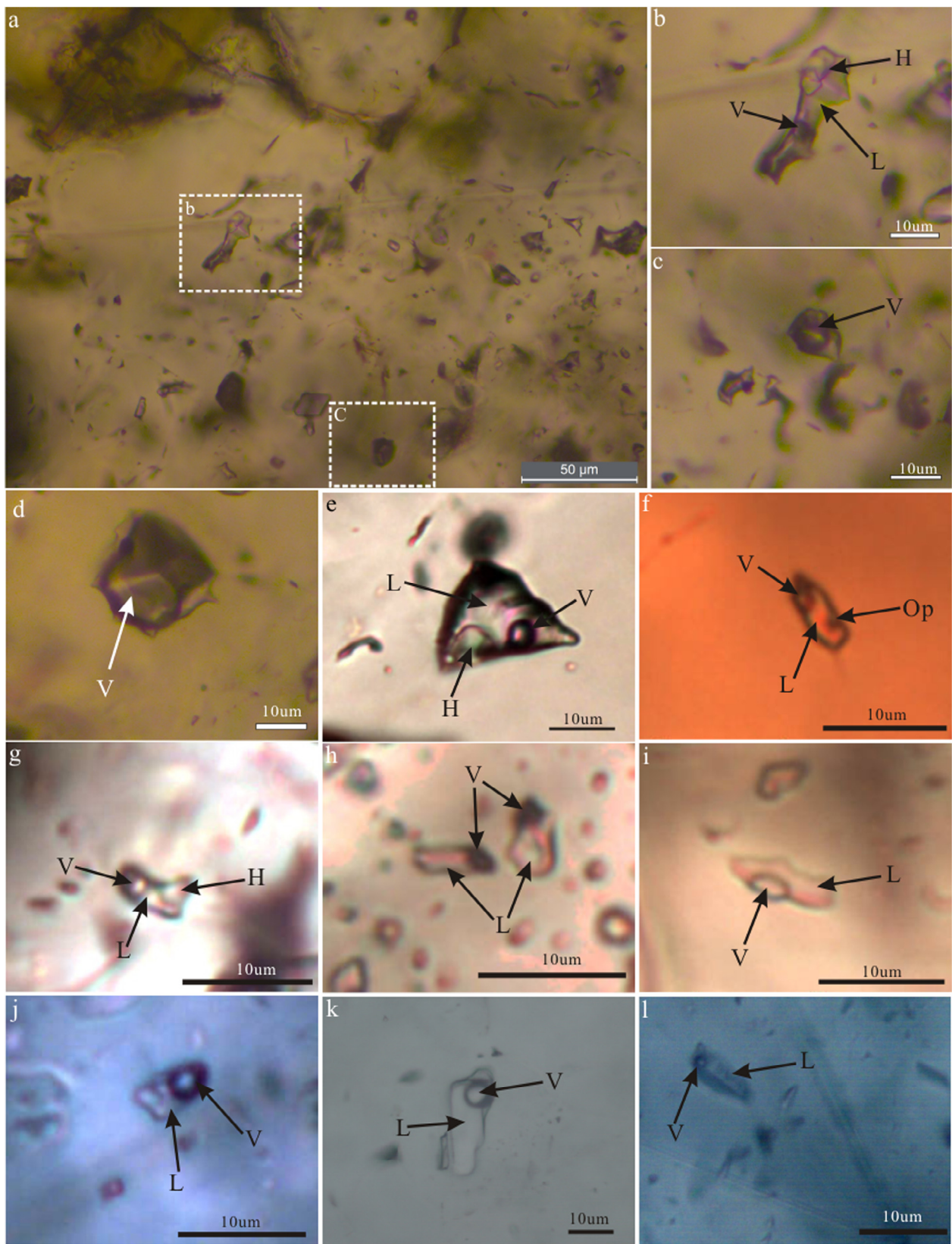


Fig. 13. Photomicrographs of representative primary fluid inclusions of different types in different stages. (a) Coexistence of primary halite-bearing and V-type fluid inclusions in prograde skarn stage garnet. (b) and (c) are closeup views for parts of (a). (d) Liquid-rich inclusion and (e) Primary inclusion containing a halite in prograde skarn stage garnet and clinopyroxene. (f) Primary inclusion containing an opaque phase and a halite (g) in prograde skarn stage garnet. (h) Two-phase aqueous inclusion in prograde skarn stage garnet. (i) and (j) Two-phase aqueous inclusions in retrograde skarn stage epidote. (k) Two-phase aqueous inclusion in quartz. (l) Two-phase aqueous inclusion in calcite.

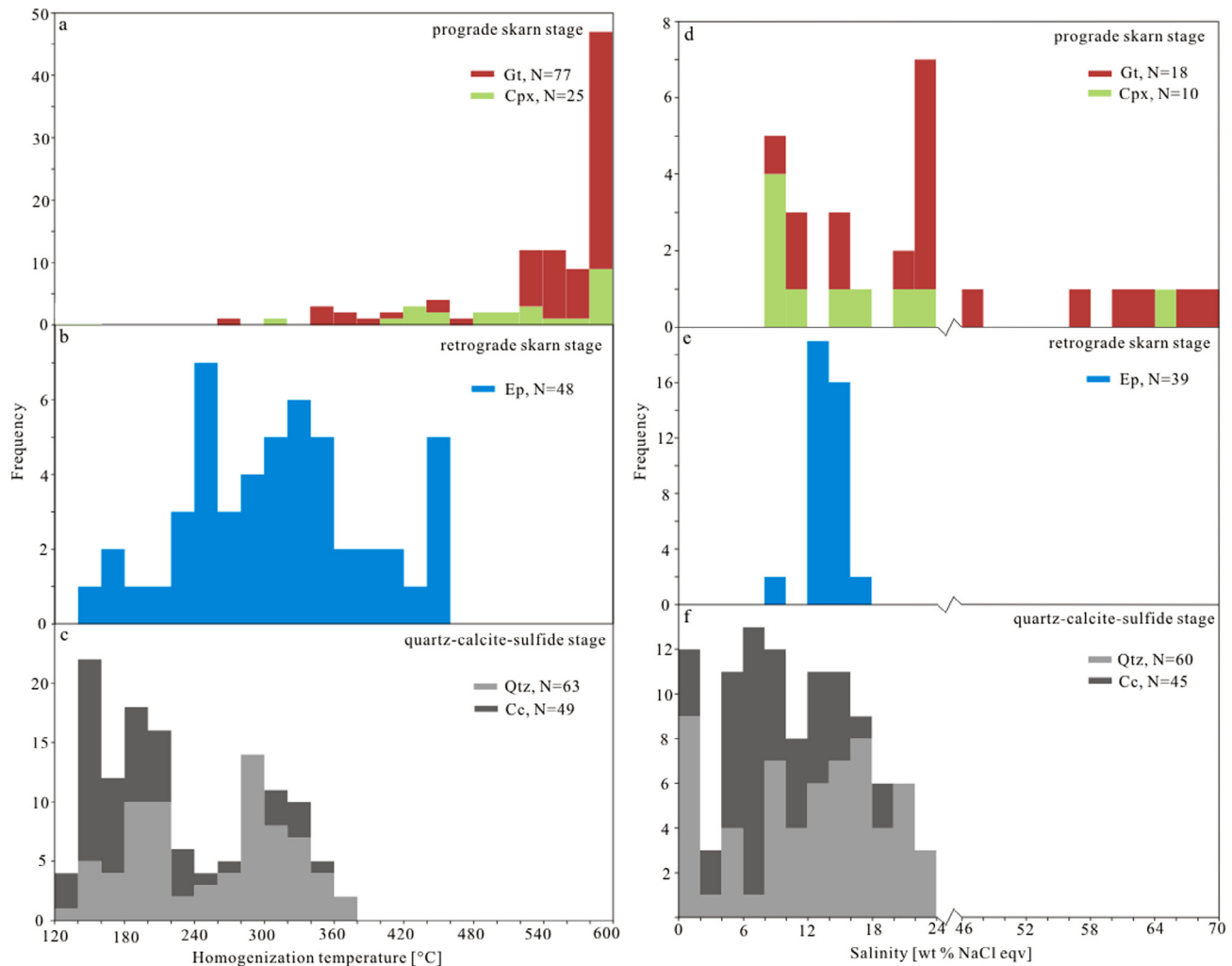


Fig. 14. Homogenization temperature (a–c) and salinity (d–f) histograms for all inclusion types separated into different stages and host minerals.

relatively high TiO_2 content ($\text{TiO}_2 > 1 \text{ wt.\%}$) magnetite have very low concentration of V_2O_3 (average $\text{V}_2\text{O}_3 = 0.02 \text{ wt.\%}$), distinct from magmatic magnetite grains directly crystallized from immiscible Fe-rich melt, which have both relatively high Ti and V contents (Fig. 11a; Nyström and Henriquez, 1994; Pang et al., 2008; Hu et al., 2014). In addition, in the $\text{Ca} + \text{Al} + \text{Mn}$ versus $\text{Ti} + \text{V}$ diagram, the main data from magnetite grains plot in the skarn type deposit area with minor data in the IOCG and porphyry type area (Fig. 11b; Dupuis and Beaudoin, 2011) instead of in the Fe-Ti-V and Kiruna-type area, which are both deposits of magmatic formation, either by crystallization from immiscible Fe-rich melt (Philpotts, 1967; Naslund, 1983; Charlier and Grove, 2012; Chen et al., 2013) or by magnetite flotation through exsolved magmatic fluid (Knipping et al. 2015a,b) respectively.

The compositional variations in hydrothermal magnetite may be governed by fluid composition-element availability, host rock buffering, re-equilibration processes, temperature, oxygen and sulfur fugacity, silicate and sulfide activity, and intrinsic crystallographic controls (Nadol et al., 2014, and references therein). All magnetite from the Cihai deposit have high Al, Si, Mg, Mn concentrations, which are comparable to magnetite expected from global skarn deposit, reflecting their elevated temperatures compared to the other types of hydrothermal magnetite and significant fluid-host rock interaction (Meinert, 1987; Nadoll et al., 2014). We interpret the gradual increasing MgO contents of magnetite in disseminated, banded to massive ores likely reflect the enhanced hydrothermal replacement (Duan et al., 2012).

Previous research has shown that titanium is an element with two characteristics: it is relatively immobile at sub-magmatic temperatures (Van Baalen, 1993) and it is compatible into magnetite (Dare et al., 2014). Our study reveals that the relative high TiO_2 content only occurs in the disseminated ores which are the products of altered diabase, and the TiO_2 content generally decreases from disseminated, banded to massive iron ores as more iron-carrying fluids developed in the system (Figs. 11a and c). Discrimination diagrams are consistent with the Cihai magnetites being of hydrothermal rather than magmatic origin (Fig. 11b). Besides, all iron oxide in the diabase protoliths are ilmenite (Zheng et al., 2017). Thus, the relatively high Ti content in some magnetite grains were likely inherited from the diabase protoliths rather than directly crystallized from iron-rich melts.

The magnetite from iron ores at the Cihai have relatively high $\delta^{18}\text{O}$ values range from +4.1 to +8.5‰ (average = 5.83‰), which are comparable to those (4.35–6.81‰; average = 5.53‰) from Ren (1985). The O isotope values of magnetite are mainly controlled by temperatures (Jonsson et al., 2013; Nyström et al., 2008). In general, magnetites from Kiruna type and Fe-Ti oxide deposits have low $\delta^{18}\text{O}$ values, which are suggested formed by magmatic high temperatures (Bilenger et al., 2016; Yu et al., 2015). By contrast, magnetites from the lower hydrothermal tem-

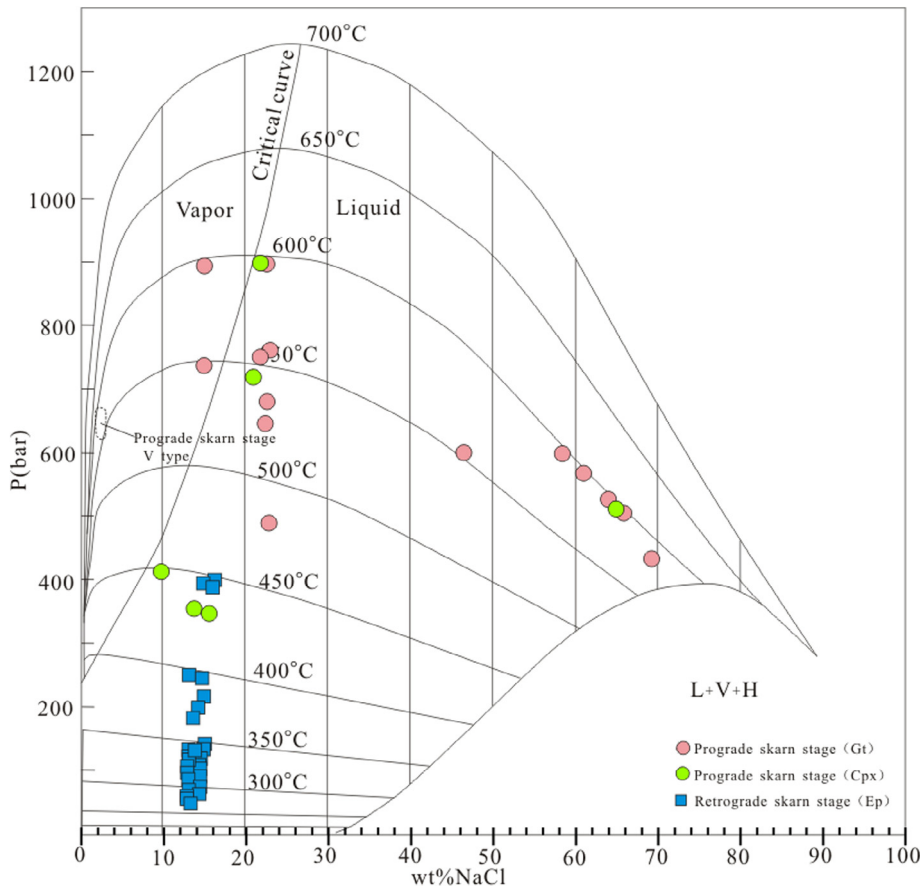


Fig. 15. NaCl-H₂O P-T-X phase diagram (after Driesner and Heinrich, 2007).

Table 4

Oxygen and hydrogen isotopic data of the Cihai deposit.

Sample	Mineral	$\delta D_{V-SMOW}/\text{‰}$	$\delta^{18}\text{O}_{V-SMOW}/\text{‰}$	Th/°C	$\delta^{18}\text{O}_{\text{fluid}}/\text{‰}$
CH13-64	Garnet	-81	7.3	543	5.37
CH13-60	Garnet	-92	6.3	570	4.49
CX13-6	Garnet	-116	7.0	560	5.15
CX13-11	Garnet	-110	7.0	526	4.99
CN13-9	Garnet	-76	10.6	541	8.66
CH12-81	Quartz	-116	12.2	244	2.96
CH12-82	Quartz	-95	12.9	163	-1.47
CH12-83	Quartz	-97	13.1	189	0.67
CH12-119	Quartz	-91	12.1	221	1.66
CH12-161	Quartz	-92	13.4	280	5.75
CH12-164	Quartz	-86	12.0	282	4.43
CH12-165	Quartz	-106	10.8	305	4.09
CN12-49	Quartz	-78	14.4	231	4.50
CN12-67	Quartz	-99	9.0	185	-3.70
CN12-68	Quartz	-91	10.8	184	-1.97
CX12-31	Quartz	-101	13.5	296	6.47
CX12-32	Quartz	-102	13.4	282	5.83

Calculated fluid compositions for garnet are based on fractionation factors of Bottinga and Javoy (1975). Calculated fluid compositions for quartz are based on fractionation factors of Clayton et al. (1972).

peratures exhibit high $\delta^{18}\text{O}$ values (Zürcher et al., 2001). As the $\delta^{18}\text{O}$ values for magnetite ores at Cihai overlap with the general range for those from hydrothermal skarn iron deposit but distinct those from magmatic iron deposits (Fig. 17). Thus, a direct role for a primary iron-oxide melts at the Cihai deposit can be ruled out on the basis of high $\delta^{18}\text{O}$ values of magnetite in both disseminated and massive iron ores.

Furthermore, our field observation reveal that multiple pulses of diabase dykes were emplaced into gabbros and Neoproterozoic

strata, and some later formed diabase dikes crosscut the early formed ore-hosted diabase and iron orebodies. In the Cihai open pit, previous studies have shown that zircon U-Pb ages of diabase documented at least three magmatic events, including 286.5 ± 1.8 Ma for ore-hosted diabase, 275.8 ± 2.2 Ma and 128.5 ± 0.3 Ma for post-ore diabase (Hou et al., 2013; Zheng et al., 2015). Thus, the sharp contact between some magnetite orebodies and diabase were likely formed by the post-ore diabase dikes that crosscut the iron orebodies.

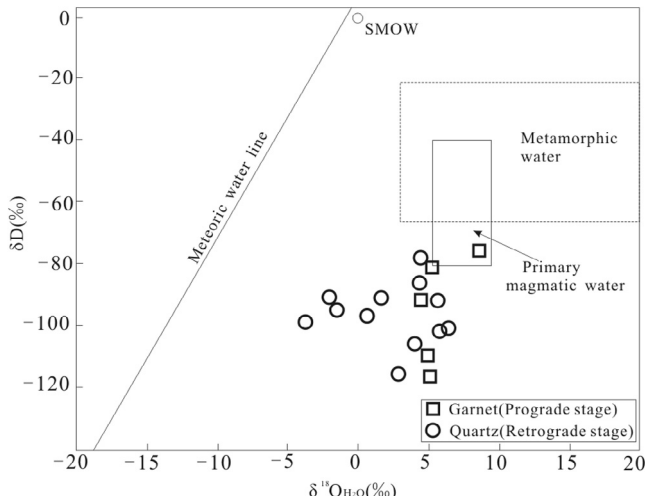


Fig. 16. Calculated oxygen and hydrogen isotopic compositions of fluids in equilibrium with garnets and quartz from the Cihai deposit. The isotopic fields for common geological waters are from Taylor (1974).

Table 5
Oxygen isotopic data of magnetite from the Cihai deposit.

Sample	Ore type	$\delta^{18}\text{O}_{\text{V-SMOW}}/‰$
CN13-8	Massive magnetite ore	7.0
CN13-9	Skarn magnetite ore	8.5
CX13-6	Skarn magnetite ore	4.1
CH13-56	Skarn magnetite ore	4.7
ZKCH13-59	Massive magnetite ore	5.3
CH13-15	Massive magnetite ore	5.4

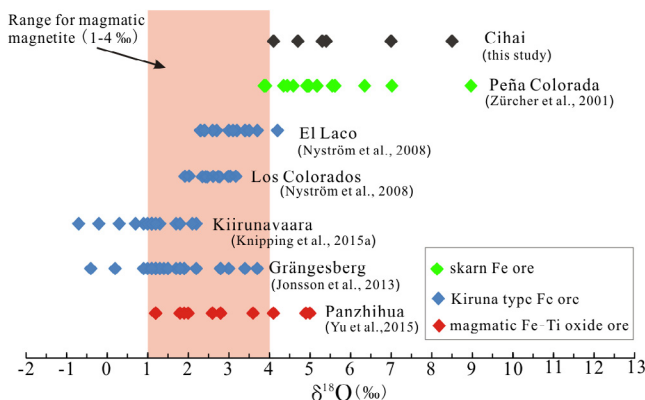


Fig. 17. Comparison of magnetite $\delta^{18}\text{O} (‰)$ in the Cihai iron deposit with those from other skarn, Kiruna-type, and magmatic Fe-Ti oxide deposits worldwide. The range of magmatic magnetites ($\delta^{18}\text{O}$ between $+1\text{‰}$ and $+4\text{‰}$) was based on Jonsson et al. (2013) and references therein.

The characteristics of the Cihai iron deposit show that: (1) pyroxene-garnet dominated skarn-like mineral assemblages are well developed in the Cihai open pit and they are closely related with disseminated magnetite (Figs. 4, 6a, 7a, b); (2) some brecciation of skarn mineral assemblages were observed in drill holes in this study (Figs. 5f and 7e), which is common in global skarn deposits (Ciobanu and Cook, 2004; Meinert et al., 2005) and has been interpreted as the mechanism responsible for initiation of pervasive infiltration (Gaspar et al., 2008); (3) massive magnetite ores are closely related to retrograde skarn minerals such as amphibole, epidote, and ilvaite (Fig. 7d, f and h), and these features are typical characteristics of skarn deposits worldwide (Einaudi et al., 2009; Shu et al., 2013).

and Burt, 1982; Kwak, 1986; Meinert et al., 2003). Accordingly, most field evidence points to hydrothermal process as the mechanism that formed the Cihai iron deposit. We therefore propose that the Cihai is a hydrothermal skarn deposit.

7.2. Fluid evolution and ore genesis

The iron origin of Cihai deposit is still unclear. Wang et al. (2006) proposed that the Cihai iron ores are closely related to the diabase. However, the geochemistry of ore-hosted diabase suggests that hydrothermal alteration has enriched iron in the diabase, rather than removed iron from the diabase (Hou et al., 2013). Therefore, the diabase is not the main source of massive iron ores. Overall, many authors consider a source at depth is the most reasonable source for massive iron ores in Cihai deposit (Sheng, 1985; Xue et al., 2000; Hou et al., 2013).

Previous research has shown that most iron skarns are closely related to granitoids (Einaudi and Burt, 1982; Meinert et al., 2005; Pons et al., 2009), we infer this may also be the case for the Cihai iron skarn on the basis of following evidences: (1) field evidence indicates the granitoid rocks have a close spatial relationship with iron skarn in examined drillholes (Fig. 5c), (2) zircon laser ablation inductively coupled plasma mass spectrometry U-Pb analyses of granitoid rocks in the Cihai open pit and drill hole yielded the age of $286.5 \pm 0.7 \text{ Ma}$ and $284.3 \pm 3.3 \text{ Ma}$ (Zheng et al., 2016c), which are closely related to the ore-forming age of massive iron ore in the Cihai open pit ($281.9 \pm 2.2 \text{ Ma}$, Zheng et al., 2015), (3) $\delta^{34}\text{S}$ values of pyrite, pyrrhotite, and chalcopyrite (-1.36 to $+4.14\text{‰}$; Ren, 1985) and δD - $\delta^{18}\text{O}$ isotopes of skarn minerals (Fig. 16) also point to a magmatic-hydrothermal origin. Thus, we suggest the Cihai deposit may associate with granitoids at depth.

In a skarn deposit, skarn minerals can provide evidence for the evolution of the hydrothermal fluid. The calculated $\delta^{18}\text{O}$ values of waters in equilibrium with garnet (4.5‰ – 8.7‰) are similar to the $\delta^{18}\text{O}$ values of the magmatic fluids (Taylor, 1974). One garnet sample has δD value which is typical of the range of compositions of igneous minerals, whereas other garnets have relatively low compositions. The relatively low δD values may record the degassing of the parental magma chamber (Suzuki and Epstein, 1976). Fluid exsolving from a granitoid magma chamber at a few kilometers depth will generally be a single-phase fluid of relatively low salinity (2–13 wt.% NaCl equiv; Audébat et al., 2008). The estimated trapping pressures for fluid inclusions in Cihai deposit are relatively low, and in magmas that crystallized at low pressure (< 1.3 kbars), the salinity of the magmatic fluid increases with increasing degree of crystallization (Audébat et al., 2008). Subsequent ascent and cooling of magma results in this fluid intersecting its solvus at a temperature of $\sim 550^\circ$ to 600°C and separate into a saline liquid phase (8–24 wt.% NaCl equiv, and >60 wt.% NaCl equiv) and a low-salinity vapor phase. Fluid inclusions trapped in prograde skarn minerals (garnet and pyroxene) recorded this phenomenon. This immiscibility between saline liquid and low-salinity vapor in prograde skarn minerals are typical of other skarn deposits worldwide (Meinert et al., 2003; Baker et al., 2004; Pons et al., 2009; Shu et al., 2013).

In the retrograde skarn stage, the fluids are cooler (220° – 456°C) and more dilute (12–16 wt.% NaCl equiv) than the fluids from prograde skarn stage. Fluid inclusions in quartz-sulfide stage quartz and calcite also record similar conditions, with temperature range from 128° to 367°C and salinity range from 0.2 to 22.9 wt.% NaCl equiv. Calculated $\delta^{18}\text{O}$ values of the fluid in equilibrium with the quartz (-3.7‰ – 6.5‰) are generally lower than the $\delta^{18}\text{O}$ values of the garnets, suggesting that significant meteoric water influx with time.

Iron mainly presents in the form of FeCl_n in a magmatic-hydrothermal system (Chou and Eugster, 1977; Boctor et al.,

Table 6

Major characteristics of the Cihai iron deposit and other iron skarns worldwide.

	Cihai	Calcic iron skarns worldwide
Size	>100 Mt	5–200 Mt, some >1000 Mt
Grade	45% Fe	~40% Fe
Metal associated	Fe, (Co)	Fe, (Cu, Co, Ni, Au)
Associated igneous rocks	Granitoids; diabase	Granitoids; some with diabase
Wall rocks	Diabase	Mostly carbonate rocks, some volcanic rocks
Early skarn minerals	Garnet, diopside, hedenbergite	Garnet, diopside, hedenbergite, and scapolite
Early stage temperature	Mostly 520–600 °C	450–690 °C
Late skarn minerals	Amphibole, epidote, ilvaite	Amphibole, epidote, actinolite, ilvaite, and chlorite
Late stage temperature	220–456 °C	370–460 °C
Other alterations	K-Na metasomatism	Extensive Na metasomatism, K metasomatism
Ore minerals	Magnetite, (pyrrhotite, cobaltite)	Magnetite, some hematite, (chalcopyrite, cobaltite, pyrrhotite, native gold)
Magnetite compositions	Mostly low Ti ($TiO_2 < 1$ wt.%); Minor high Ti ($TiO_2 > 1$ wt.%); Some high Si ($SiO_2 > 1$ wt.%)	Mostly low Ti ($TiO_2 < 1$ wt.%); Some high Si ($SiO_2 > 1$ wt.%)
Magnetite O isotopes	$\delta^{18}O$ 4.1–8.5‰	$\delta^{18}O$ 3.87–8.97‰
Tectonic setting	Post-collision extension environment	Oceanic island arc; active continental margin

Major characteristics of the iron skarns worldwide are from Einaudi and Burt, 1982; Meinert, 1984; Zürcher et al., 2001; Meinert et al. (2005); Pons et al. (2009); Jansson and Allen, 2013; Hu et al. (2014).

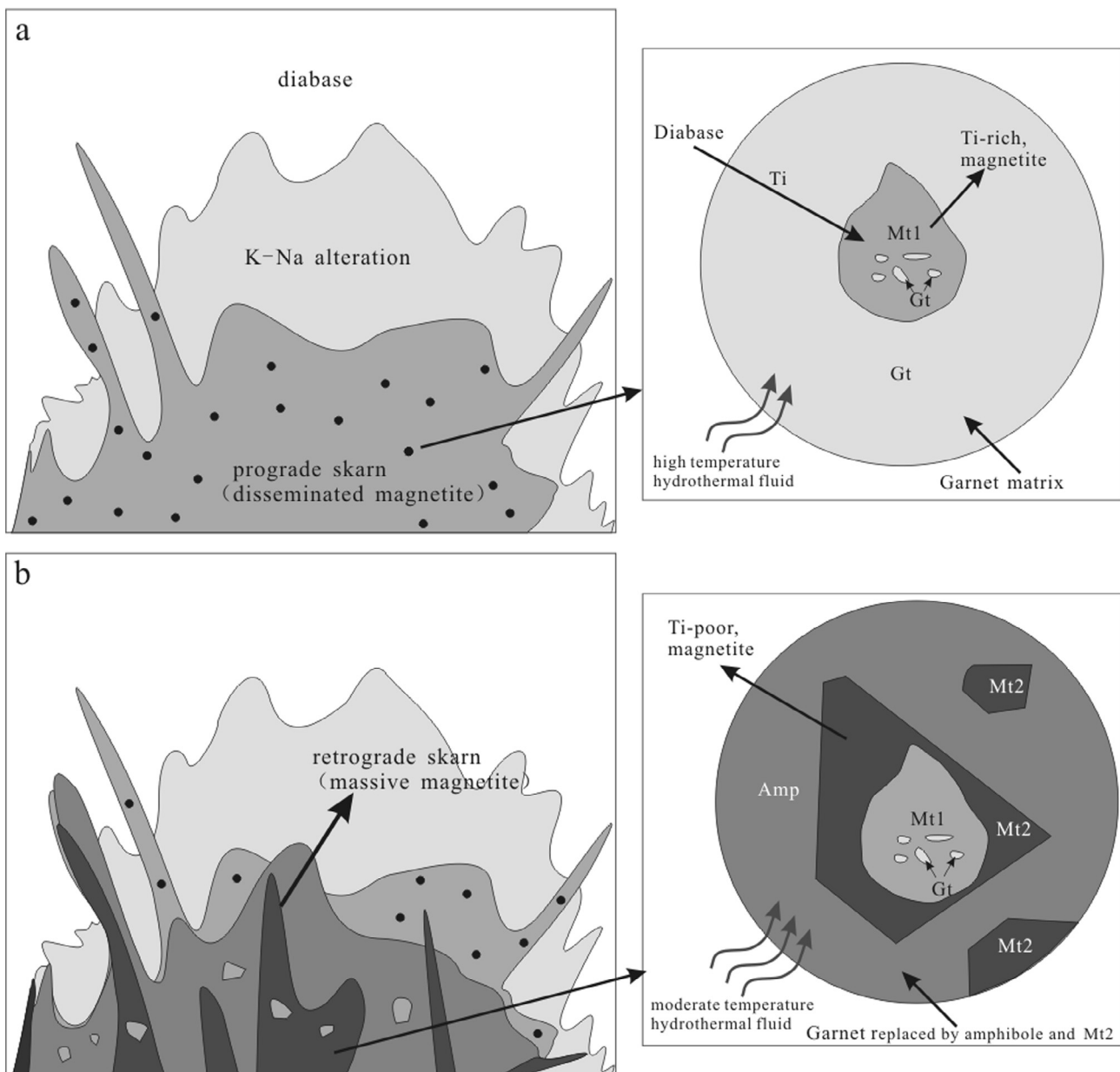


Fig. 18. Schematic representation of the Cihai skarn hydrothermal system, including formation of high-Ti magnetite (Mt_1) and low-Ti (Mt_2) magnetite.

1980; Baker et al., 2004). The presence of disseminated magnetite and high salinity fluids (up to >60 wt.% NaCl equiv) at high-temperature (homogenization temperatures up to 600 °C) in the early prograde skarn stage indicates that these fluids were capable of transporting abundant iron in solution. During the prograde skarn stage, some disseminated magnetites with high Ti content were formed by inheriting Ti from the diabase protoliths (Fig. 18a). By contrast, the fluid inclusions in epidote associated with the massive iron ore indicate lower temperature (220°–456 °C) and lower salinity (8.4–16.3 wt.% NaCl equiv) fluids at hydrostatic pressures during the retrograde skarn stage. Experiments on Fe solubility under these conditions (Simon et al., 2004) indicate that a decrease in temperature and salinity documented for the Cihai skarn system would cause a notable decrease in iron solubility and massive magnetite precipitation. Consequently, massive magnetites with low Ti content were formed at the retrograde stage (Fig. 18b).

7.3. Comparison with other skarn Fe deposits worldwide

Skarns in the Cihai deposit are similar to other calcic Fe skarn deposits worldwide (Table 6; Einaudi and Burt, 1982; Meinert, 1984; Zürcher et al., 2001; Pons et al., 2009) since they have several main features common to other Fe skarns: (1) the size, ore grade, associated metal, and related igneous rocks of the Cihai iron deposit are similar to those from other calcic skarn Fe deposits, (2) two typical skarn alteration types, including an early prograde skarn alteration with anhydrous minerals, such as garnet, diopside, and hedenbergite, and a later retrograde skarn alteration with hydrous minerals, such as amphibole, epidote, and ilvaite plus massive iron ore minerals, (3) the prograde skarn alteration forms from relatively high temperature, high salinity liquid, whereas the retrograde skarn alteration forms from lower temperature, lower salinity fluids, (4) the Na and K metasomatism were well developed, (5) magnetite is the predominant iron ore mineral, the most important iron orebodies are associated with retrograde mineral assemblages and disseminated iron ores are associated with prograde skarn minerals, (6) most magnetite grains have similar low Ti content and relatively high $\delta^{18}\text{O}$ value, (7) overall, skarn minerals include garnet, diopside, and amphibole in the Cihai Fe deposit display compositions similar to those from other calcic skarn Fe deposits.

Nonetheless, several features of the Cihai Fe skarn deposit differ from other Fe skarns: (1) iron ores are hosted in the diabase, (2) some magnetite grains exhibit relatively high TiO₂ content, (3) and the deposit was formed in a post-collision extension environment (Zheng et al., 2015).

8. Conclusions

- The Cihai Fe deposit is hosted in the diabase, and contains vein and lenticular orebodies. The ore-forming process comprises: K-Na alteration stage (I), prograde skarn stage (II), retrograde skarn stage (III), and quartz–calcite–sulfide stage (IV). Magnetite is the predominant iron ore mineral, Fe mineralization formed during stages (II) and (III).
- Overall, skarn minerals include garnet, diopside, and amphibole in the Cihai Fe deposit display compositions similar to those from other skarn Fe deposits. Some relatively high Ti content in some magnetite grains may be inherited from the diabase protoliths rather than directly crystallized from iron-rich melts because V concentration in these grains are much lower than observed in magmatic magnetite grains. The $\delta^{18}\text{O}$ values of magnetite ores are similar to values reported in other skarn Fe deposits but distinct from those of other Kiruna-type and magmatic Fe-Ti-V deposits worldwide.

- The prograde skarn stage indicates high temperature (cluster in 520–600 °C) and moderate- to high-salinity (8–24 wt.% NaCl equiv, and >60 wt.% NaCl equiv) fluids. In comparison, the retrograde stage reveals lower temperature (cluster in 220–460 °C) and salinity (12–16 wt.% NaCl equiv) fluids. Quartz–calcite–sulfide stage shows fluids of lower temperature (cluster in 150–250 °C) and variable salinity (0.2–22 wt.% NaCl equiv). H-O isotope compositions indicate that the prograde skarn stage comprises dominantly magmatic fluids, and significant meteoric water influx with time. A decrease in temperature and salinity documented for the Cihai skarn system would cause a notable decrease in iron solubility and massive magnetite precipitation.
- The geology, mineral assemblages and compositions, ore genesis, and hydrothermal evolution processes of the Cihai Fe skarn deposit are similar to many other calcic Fe skarns that have been documented worldwide. Taken together, we suggest that the Cihai is a typical Fe skarn deposit rather than is associated with iron-rich melts as previously suggested.

Acknowledgments

Critical reviews from two reviewers (Dr. Jaayke Knipping and anonymous) and suggestions from the Editor-in-Chief, Prof. Franco Pirajno, are greatly appreciated. We are grateful to Dr. Tim Baker, Anthony Reid, and Prof. Larry Meinert, who made constructive comments and helped to improve the language on an early version of our manuscript. This research was jointly supported by the Ministry of Land and Resources Public Welfare Industry Special Funds for Scientific Research Project (Grant No. 201211073), the National Basic Research Program of China (No. 2012CB416803), the China Postdoctoral Science Foundation (No. 2016LH0003), and NSFC (No. 41372062 and 41672047). We thank Feng Liu and Qiang Li for their help during the field work.

Appendix A. Supplementary data

Supplementary data associated with this article can be found, in the online version, at <http://dx.doi.org/10.1016/j.oregeorev.2017.01.032>.

References

- Audétat, A., Pettke, T., Heinrich, C.A., Bodnar, R.J., 2008. Special paper: the composition of magmatic-hydrothermal fluids in barren and mineralized intrusions. *Econ. Geol.* 103 (5), 877–908.
- Baker, T., Achterberg, E.V., Ryan, C.G., Lang, J.R., 2004. Composition and evolution of ore fluids in a magmatic-hydrothermal skarn deposit. *Geology* 32 (2), 117–120.
- Bilenger, L.D., Simon, A.C., Reich, M., Lundstrom, C.C., Gajos, N., Bindeman, I., Barra, F., Munizaga, R., 2016. Fe–O stable isotope pairs elucidate a high-temperature origin of Chilean iron oxideapatite deposits. *Geochim. Cosmochim. Acta* 177, 94–104.
- Boctor, N.Z., Popp, R.K., Frantz, J.D., 1980. Mineral-solution equilibria-IV. Solubilities and the thermodynamic properties of Fe_2O_3 in the system $\text{Fe}_2\text{O}_3 - \text{H}_2\text{O} - \text{HCl}$. *Geochim. Cosmochim. Acta* 44, 1509–1518.
- Bodnar, R.J., 1993. Revised equation and table for determining the freezing point depression of $\text{H}_2\text{O}-\text{NaCl}$ solutions. *Geochim. Cosmochim. Acta* 57, 683–684.
- Bottinga, V., Javoy, M., 1975. Oxygen isotope partitioning among the minerals in igneous and metamorphic rocks. *Rev. Geophys.* 13, 401–418.
- Chai, F., Mao, J., Dong, L., Yang, F., Liu, F., Geng, X., Zhang, Z., 2009. Geochronology of metarhyolites from the Kangbutieba Formation in the Kelang basin, Altay Mountains, Xinjiang: implications for the tectonic evolution and metallogeny. *Gondwana Res.* 16 (2), 189–200.
- Charlier, B., Grove, T.L., 2012. Experiments on liquid immiscibility along tholeiitic liquid lines of descent. *Contrib. Miner. Petrol.* 164 (1), 27–44.
- Chen, Y.C., Liu, D.Q., Tang, Y.L., Wang, D.H., Dong, L.H., Xu, X., Wang, X.D., 2008. Mineral Resources and Mineralization System in Tianshan, China (Book 1). Geological Publishing House, Beijing, pp. 246–287 (in Chinese with English abstract).
- Chen, W.T., Zhou, M.F., Zhao, T.P., 2013. Differentiation of nelsonitic magmas in the formation of the ~ 1.74 Ga Damiao Fe-Ti-P ore deposit, North China. *Contrib. Miner. Petrol.* 165 (6), 1341–1362.

- Chou, I.M., Eugster, H.P., 1977. Solubility of magnetite in supercritical chloride solutions. *Am. J. Sci.* 277 (10), 1296–1314.
- Ciobanu, C.L., Cook, N.J., 2004. Skarn textures and a case study: the Ocna de Fier-Dogenecea orefield, Banat, Romania. *Ore Geol. Rev.* 24 (3), 315–370.
- Clayton, R.N., Mayeda, T.K., 1963. The use of bromine pentafluoride in the extraction of oxygen from oxides and silicates for isotopic analysis. *Geochim. Cosmochim. Acta* 27, 43–52.
- Clayton, R.N., O'Neil, J.R., Mayeda, T.K., 1972. Oxygen isotope exchange between quartz and water. *J. Geophys. Res.* 77, 3057–3067.
- Coleman, M.L., Sheppard, T.J., Durham, J.J., Rouse, J.E., Moore, G.R., 1982. Reduction of water with zinc for hydrogen isotope analysis. *Anal. Chem.* 54, 993–995.
- Dare, S.A., Barnes, S.J., Beaudoin, G., Méric, J., Boutroy, E., Potvin-Doucet, C., 2014. Trace elements in magnetite as petrogenetic indicators. *Miner. Deposita* 49, 785–796.
- Driesner, T., Heinrich, C.A., 2007. The system $H_2O-NaCl$. Part I: correlation formulae for phase relations in temperature-pressure-composition space from 0 to $1000^\circ C$, 0 to 5000 bar, and 0 to 1 X NaCl. *Geochim. Cosmochim. Acta* 71 (20), 4880–4901.
- Duan, C., Li, Y.H., Yuan, S.D., Hu, M.Y., Zhao, L.H., Chen, X.D., Zhang, C., Liu, J.L., 2012. Geochemical characteristics of magnetite from Washan iron deposit in Ningwu ore district and its constraints on ore-forming. *Acta Petrol. Sin.* 28, 243–257 (in Chinese with English abstract).
- Duan, S.G., Zhang, Z.H., Jiang, Z.S., Zhao, J., Zhang, Y.P., Li, F.M., Tian, J.Q., 2013. Geology, geochemistry, and geochronology of the Dunde iron-zinc ore deposit in western Tianshan, China. *Ore Geol. Rev.* 57 (3), 441–461.
- Dupuis, C., Beaudoin, G., 2011. Discriminant diagrams for iron oxide trace element fingerprinting of mineral deposit types. *Miner. Deposita* 46, 319–335.
- Einaudi, M.T., Burt, D.M., 1982. Introduction; terminology, classification, and composition of skarn deposits. *Econ. Geol.* 77 (4), 745–754.
- Friedman, I., O'Neil, J.R., 1977. Complication of stable isotope fractionation factors of geochemical interest in data of geochemistry. In: Fleischer, M. (Ed.), Geological Professional Paper. 6th ed., U.S. Geological Survey, p. 440.
- Gaspar, M., Knaack, C., Meinert, L.D., Moretti, R., 2008. REE in skarn systems: A LA-ICP-MS study of garnets from the Crown Jewel gold deposit. *Geochim. Cosmochim. Acta* 72 (1), 185–205.
- Goldfarb, R.J., Taylor, R.D., Collins, G.S., Goryachev, N.A., Orlandini, O.F., 2014. Phanerozoic continental growth and gold metallogeny of Asia. *Gondwana Res.* 25 (1), 48–102.
- Han, B.F., Guo, Z.J., Zhang, Z.C., Zhang, L., Chen, J.F., Song, B., 2010. Age, geochemistry, and tectonic implications of a late Paleozoic stitching pluton in the North Tian Shan suture zone, western China. *Geol. Soc. Am. Bull.* 122 (3–4), 627–640.
- Hedenquist, J.W., Arriba, A., Reynolds, T.J., 1998. Evolution of intrusion-centered hydrothermal system: far Southeast-Lepanto porphyry and epithermal Cu-Au deposits, Philippines. *Econ. Geol.* 93, 373–404.
- Hong, W., Zhang, Z.H., Huaqin, L.I., Fengming, L.I., Liu, X.Z., 2012. Metallogenic epoch of Chaganguo iron deposit in western Tianshan Mountains, Xinjiang: information for garnet Sm-Nd isochron age. *Miner. Deposits* 31, 1067–1074 (in Chinese with English abstract).
- Hou, T., Zhang, Z.C., Kusky, T., 2011. Gushan magnetite-apatite deposit in the Ningwu basin, Lower Yangtze River Valley, SE China: hydrothermal or Kiruna-type? *Ore Geol. Rev.* 43 (1), 333–346.
- Hou, T., Zhang, Z.C., Santosh, M., Encarnacion, J., Wang, M., 2013. The Cihai diabase in the Beishan region, NW China: isotope geochronology, geochemistry and implications for Cornwall-style iron mineralization. *J. Asian Earth Sci.* 70, 231–249.
- Hou, T., Zhang, Z.C., Santosh, M., Encarnacion, J., Zhu, J., Luo, W.J., 2014. Geochronology and geochemistry of submarine volcanic rocks in the Yamansu iron deposit, Eastern Tianshan Mountains, NW China: constraints on the metallogenesis. *Ore Geol. Rev.* 56, 487–502.
- Hu, H., Li, J.W., Lentz, D., Ren, Z., Zhao, X.F., Deng, X.D., Hall, D., 2014. Dissolution-reprecipitation process of magnetite from the Chengchao iron deposit: insights into ore genesis and implication for in-situ chemical analysis of magnetite. *Ore Geol. Rev.* 57, 393–405.
- Hu, H., Lentz, D., Li, J.W., McCarron, T., Zhao, X.F., Hall, D., 2015. Reequilibration processes in magnetite from iron skarn deposits. *Econ. Geol.* 110 (1), 1–8.
- Huang, X.W., Zhou, M.F., Qi, L., Gao, J.F., Wang, Y.W., 2013. Re-Os isotopic ages of pyrite and chemical composition of magnetite from the Cihai magmatic-hydrothermal Fe deposit, NW China. *Miner. Deposita* 48 (8), 925–946.
- Huang, X.W., Liang, Q.I., Wang, Y.C., Liu, Y.Y., 2014. Re-Os dating of magnetite from the Shaquanzi Fe-Cu deposit, eastern Tianshan, NW China. *Sci. China Earth Sci.* 57 (2), 267–277.
- Huang, X.W., Gao, J.F., Qi, L., Zhou, M.F., 2015. In-situ LA-ICP-MS trace elemental analyses of magnetite and Re-Os dating of pyrite: the Tianhu hydrothermally remobilized sedimentary Fe deposit, NW China. *Ore Geol. Rev.* 65, 900–916.
- Huberty, J.M., Konishi, H., Heck, P.R., Fournelle, J.H., Valley, J.W., Xu, H., 2012. Silician magnetite from the Dales Gorge Member of the Brockman Iron Formation, Hamersley Group, Western Australia. *Am. Miner.* 97 (1), 26–37.
- Jahn, B.M., Wu, F.Y., Chen, B., 2000. Granitoids of the Central Asian Orogenic Belt and continental growth in the Phanerozoic: transactions of the Royal Society of Edinburgh. *Earth Sci.* 91 (1–2), 181–193.
- Jansson, N.F., Allen, R.L., 2013. Timing and setting of skarn and iron oxide formation at the Smålfarmossen calcic iron skarn deposit, Bergslagen, Sweden. *Miner. Deposita* 48 (3), 313–339.
- Jiang, Z.S., Zhang, Z.H., Wang, Z.H., Duan, S.G., Li, F.M., Tian, J.Q., 2014. Geology, geochemistry, and geochronology of the Zhibo iron deposit in the Western Tianshan, NW China: constraints on metallogenesis and tectonic setting. *Ore Geol. Rev.* 57, 406–424.
- Jonsson, E., Troll, V.R., Högdahl, K., Harris, C., Weis, F., Nilsson, K.P., Skelton, A., 2013. Magmatic origin of giant 'Kiruna-type'apatite-iron-oxide ores in Central Sweden. *Sci. Rep.* <http://dx.doi.org/10.1038/srep01644>.
- Knipping, J.L., Bilenker, L.D., Simon, A.C., Reich, M., Barra, F., Deditius, A.P., Wölle, M., Heinrich, C.A., Holtz, F., Munizaga, R., 2015a. Trace elements in magnetite from massive iron oxide-apatite deposits indicate a combined formation by igneous and magmatic-hydrothermal processes. *Geochim. Cosmochim. Acta* 171, 15–38.
- Knipping, J.L., Bilenker, L.D., Simon, A.C., Reich, M., Barra, F., Deditius, A.P., Lundstrom, C., Bindeman, I., Munizaga, R., 2015b. Giant Kiruna-type deposits form by efficient flotation of magmatic magnetite suspensions. *Geology* 43 (7), 591–594.
- Kröner, A., Kovach, V., Belousova, E., Hegner, E., Armstrong, R., Dolgopolova, Seltmann, S., Alexeev, D.V., Hoffmann, J.E., Wong, J., Sun, M., Cai, K.D., Wang, T., Tong, Y., Wilde, S.A., Degtyarev, K.E., Rytisk, E., 2014. Reassessment of continental growth during the accretionary history of the Central Asian Orogenic Belt. *Gondwana Res.* 25 (1), 103–125.
- Kwak, T.A.P., 1986. Fluid inclusions in skarns (carbonate replacement deposits). *J. Metamorph. Geol.* 4 (4), 363–384.
- Li, H.M., Ding, J.H., Zhang, Z.C., Li, L.X., Chen, J., Yao, T., 2015. Iron-rich fragments in the Yamansu iron deposit, Xinjiang, NW China: constraints on metallogenesis. *J. Asian Earth Sci.* 113, 1068–1081.
- Mao, J.W., Kerrich, R., Li, H., Li, Y., 2002. High $^3He/ ^4He$ ratios in the Wanglu gold deposit, Hunan Province, China: implications for mantle fluids along the Tanlu deep fault zone. *Geochim. J.* 36, 197–208.
- Mao, J.W., Yang, J.M., Du, A.D., Han, C.M., Wang, Z.L., 2003. Re-Os age of Cu-Ni ores from the Huangshandong Cu-Ni sulfide deposit in East Tianshan and its geodynamic significance. *Acta Geol. Sin.* 77 (2), 220–226.
- Mao, J.W., Goldfarb, R.J., Wang, Y.T., Hart, C.J., Wang, Z.L., Yang, J.M., 2005. Late Paleozoic base and precious metal deposits, East Tianshan, Xinjiang, China: characteristics and geodynamic setting. *Episodes* 28 (1), 23–36.
- Mao, J.W., Pirajno, F., Zhang, Z.H., Chai, F.M., Wu, H., Chen, S.P., Cheng, L.S., Yang, J.M., Zhang, C.Q., 2008. A review of the Cu-Ni sulphide deposits in the Chinese Tianshan and Altay orogens (Xinjiang Autonomous Region, NW China): principal characteristics and ore-forming processes. *J. Asian Earth Sci.* 32, 184–203.
- McCrea, M., 1950. On the isotopic chemistry of carbonates and a paleotemperature scale. *J. Chem. Phys.* 18 (6), 849–857.
- Meinert, L.D., 1984. Mineralogy and petrology of iron skarns in western British Columbia, Canada. *Econ. Geol.* 79 (5), 869–882.
- Meinert, L.D., 1987. Skarn zonation and fluid evolution in the Groundhog mine, Central mining district, New Mexico. *Econ. Geol.* 82 (3), 523–545.
- Meinert, L.D., Hedenquist, J.W., Satoh, H., Matsuhisa, Y., 2003. Formation of anhydrous and hydrous skarn in Cu-Au ore deposits by magmatic fluids. *Econ. Geol.* 98 (1), 147–156.
- Meinert, L.D., Dipple, G.M., Niculescu, S., 2005. World skarn deposits: Economic Geology, 100th Anniversary Volume: 299–336.
- Nadoll, P., Mauk, J.L., Hayes, T.S., Koenig, A.E., Box, S.E., 2012. Geochemistry of magnetite from hydrothermal ore deposits and host rocks of the Mesoproterozoic Belt Supergroup, United States. *Econ. Geol.* 107 (6), 1275–1292.
- Nadoll, P., Angerer, T., Mauk, J.L., French, D., Walshe, J., 2014. The chemistry of hydrothermal magnetite: a review. *Ore Geol. Rev.* 61, 1–32.
- Naslund, H.R., 1983. The effect of oxygen fugacity on liquid immiscibility in iron-bearing silicate melts. *Am. J. Sci.* 283 (10), 1034–1059.
- Newberry, N.G., Peacor, D.R., Essene, E.J., Geissman, J.W., 1982. Silicon in magnetite: high resolution microanalysis of magnetite-ilmenite intergrowths. *Contrib. Miner. Petrol.* 80 (4), 334–340.
- Nyström, J.O., Henriquez, F., 1994. Magmatic features of iron ores of the Kiruna type in Chile and Sweden; ore textures and magnetite geochemistry. *Econ. Geol.* 89 (4), 820–839.
- Nyström, J.O., Billstrom, K., Henriquez, F., Fallick, A.E., Naslund, H.R., 2008. Oxygen isotope composition of magnetite in iron ores of the Kiruna type in Chile and Sweden. *GFF* 130, 177–188.
- Pang, K.N., Zhou, M.F., Lindsley, D., Zhao, D., Malpas, J., 2008. Origin of Fe-Ti oxide ores in mafic intrusions: evidence from the Panzhihua intrusion, SW China. *J. Petrol.* 49 (2), 295–313.
- Philpotts, A.R., 1967. Origin of certain iron-titanium oxide and apatite rocks. *Econ. Geol.* 62 (3), 303–315.
- Pirajno, F., Mao, J.W., Zhang, Z.C., Zhang, Z.H., Chai, F.M., 2008. The association of mafic-ultramafic intrusions and A-type magmatism in the Tian Shan and Altay orogens, NW China: implications for geodynamic evolution and potential for the discovery of new ore deposits. *J. Asian Earth Sci.* 32 (2), 165–183.
- Pons, J.M., Franchini, M., Meinert, L., Recio, C., Etcheverry, R., 2009. Iron Skarns of the Vegas Peladas District, Mendoza, Argentina. *Econ. Geol.* 104 (2), 157–184.
- Qin, K.Z., Su, B.X., Sakyi, P.A., Tang, D.M., Li, X.H., Sun, H., Xiao, Q.H., Liu, P.P., 2011. SIMS zircon U-Pb geochronology and Sr-Nd isotopes of Ni-Cu-bearing mafic-ultramafic intrusions in eastern Tianshan and Beishan in correlation with flood basalts in Tarim Basin (NW China): constraints on a ca. 280 Ma mantle plume. *Am. J. Sci.* 311 (3), 237–260.
- Ren, F.G., 1985. Characteristic of sulfur isotope composition from some iron deposit (mineral occurrence) in Tianshan Mountain area, Eastern Xinjiang Uygur Ziziqu (autonomous region) and discussion on some related problems. *Bull. Tianjin Inst. Geol. Min. Res.* 13, 49–62 (in Chinese with English abstract).

- Roedder, E., Bodnar, R.J., 1980. Geologic pressure determinations from fluid inclusion studies. *Annu. Rev. Earth Planet. Sci.* 8, 263–301.
- Rose, A.W., Herrick, D.C., Deines, P., 1985. An oxygen and sulfur isotope study of skarn-type magnetite deposits of the Cornwall type, southeastern Pennsylvania. *Econ. Geol.* 80 (2), 418–443.
- Rusk, B., Reed, M., Dilles, J., 2008. Fluid inclusion evidence for magmatic-hydrothermal fluid evolution in the porphyry copper-molybdenum deposit at Butte, Montana. *Econ. Geol.* 103 (2), 307–334.
- Ryabchikov, I.D., Kogarko, L.N., 2006. Magnetite compositions and oxygen fugacities of the Khibina magmatic system. *Lithos* 91 (1), 35–45.
- Sheng, J.F., 1985. Mineralization and alteration of the Cihai iron deposit: bulletin of the Institute of Mineral Deposits. *Chin. Acad. Geol. Sci.* 3, 89–109 (in Chinese with English abstract).
- Shepherd, J.P., Rankins, A.H., Alderton, D.H.M., 1985. *A Practical Guide to Fluid Inclusion Studies*. Blackie and Sons Ltd., Glasgow, p. 239.
- Shimazaki, H., 1998. On the occurrence of silician magnetites. *Resour. Geol.* 48 (1), 23–29.
- Shu, Q.H., Lai, Y., Sun, Y., Wang, C., Meng, S., 2013. Ore genesis and hydrothermal evolution of the Baiyinuo'er zinc-lead skarn deposit, Northeast China: evidence from isotopes (S, Pb) and fluid inclusions. *Econ. Geol.* 108 (4), 835–860.
- Simon, A.C., Pettke, T., Candela, P.A., Piccoli, P.M., Heinrich, C.A., 2004. Magnetite solubility and iron transport in magmatic-hydrothermal environments. *Geochim. Cosmochim. Acta* 68 (23), 4905–4914.
- Su, B.X., Qin, K.Z., Sakyi, P.A., Li, X.H., Yang, Y.H., Sun, H., Tang, D.M., Liu, P.P., Xiao, Q.H., Malaviarachchi, S.P., 2011. U-Pb ages and Hf-O isotopes of zircons from Late Paleozoic mafic-ultramafic units in the southern Central Asian Orogenic Belt: tectonic implications and evidence for an Early-Permian mantle plume. *Gondwana Res.* 20 (2), 516–531.
- Su, B.X., Qin, K.Z., Sun, H., Tang, D.M., Sakyi, P.A., Chu, Z.Y., Liu, P.P., Xiao, Q.H., 2012. Subduction-induced mantle heterogeneity beneath Eastern Tianshan and Beishan: insights from Nd-Sr-Hf-O isotopic mapping of Late Paleozoic mafic-ultramafic complexes. *Lithos* 134, 41–51.
- Suzuoki, T., Epstein, S., 1976. Hydrogen isotope fractionation between OH-bearing minerals and water. *Geochim. Cosmochim. Acta* 40, 1229–1240.
- Tang, P.Z., Wang, J.B., Wang, Y.W., Long, L.L., 2010. Geochemical characteristics of mafic-ultramafic rocks in the Cihai ore district, Xinjiang, and their geological significance. *Geochimica* 39, 542–552 (in Chinese with English abstract).
- Taylor, H.P., 1974. The application of oxygen and hydrogen isotope studies to problems of hydrothermal alteration and ore deposition. *Econ. Geol.* 69 (6), 843–883.
- Van Baalen, M.R., 1993. Titanium mobility in metamorphic systems: a review. *Chem. Geol.* 110 (1), 233–249.
- Wang, Y.W., Sha, J.M., Cheng, C., 2006. Composition of magnetite from the Cihai Fe (Co) deposit, Xinjiang, and its genetic significance. *Miner. Deposits* 25, 321–324 (in Chinese).
- Wang, D.H., Chen, S.P., Wang, H., Meng, X.G., Chen, Z.H., Wang, C.H., Li, C.J., 2007. Mineralization pedigree and prospecting for iron deposits in eastern Tianshan. *Geotectonica Et Metallogenica* 31 (2), 186–192 (in Chinese with English abstract).
- Westendorp, R.W., Watkinson, D.H., Jonasson, I.R., 1991. Silicon-bearing zoned magnetite crystals and the evolution of hydrothermal fluids at the Ansil Cu-Zn mine, Rouyn-Noranda, Quebec. *Econ. Geol.* 86 (5), 1110–1114.
- Windley, B.F., Alexeiev, D., Xiao, W.J., Kröner, A., Badarch, G., 2007. Tectonic models for accretion of the Central Asian Orogenic belt. *J. Geol. Soc.* 164, 31–47.
- Xiao, W.J., Zhang, L.C., Qin, K.Z., Sun, S., Li, J.L., 2004. Paleozoic accretionary and collisional tectonics of the eastern Tianshan (China): implications for the continental growth of central Asia. *Am. J. Sci.* 304 (4), 370–395.
- Xie, G.Q., Mao, J.W., Zhao, H., Duan, C., Yao, L., 2012. Zircon U-Pb and phlogopite 40Ar-39Ar age of the Chengchao and Jinshandian skarn Fe deposits, southeast Hebei Province, Middle-Lower Yangtze River Valley metallogenic belt, China. *Miner. Deposita* 47 (6), 633–652.
- Xue, C.J., Ji, J.S., Yang, Q.J., 2000. Subvolcanic hydrothermal metallogenesis of the Chai iron (cobalt) deposit, Xinjiang. *Miner. Deposits* 19 (2), 156–164 (in Chinese with English abstract).
- Yang, F.Q., Mao, J.W., Liu, F., Chai, F.M., Geng, X.X., Zhang, Z.X., Guo, X.J., Liu, G.R., 2013. A review of the geological characteristics and mineralization history of iron deposits in the Altay orogenic belt of the Xinjiang, Northwest China. *Ore Geol. Rev.* 54, 1–16.
- Yang, F., Chai, F., Zhang, Z., Geng, X., Li, Q., 2014. Zircon U-Pb geochronology, geochemistry, and Sr-Nd-Hf isotopes of granitoids in the Yulekenhalasu copper ore district, northern Junggar, China: petrogenesis and tectonic implications. *Lithos* 190, 85–103.
- Yu, S.Y., Song, X.Y., Ripley, E.M., Li, C., Chen, L.M., She, Y.W., Luan, Y., 2015. Integrated O-Sr-Nd isotope constraints on the evolution of four important Fe-Ti oxide ore-bearing mafic-ultramafic intrusions in the Emeishan large igneous province, SW China. *Chem. Geol.* 401, 28–42.
- Zhang, Z.Z., Gu, L.X., Wu, C.Z., Li, W.Q., Xi, A.H., Wang, S., 2005. Zircon SHRIMP dating for the Weiya pluton, eastern Tianshan: its geological implications. *Acta Geol. Sin.* 79 (4), 481–490.
- Zhang, Z.C., Hou, T., Santosh, M., Li, H.M., Li, J.W., Zhang, Z.H., Song, X.Y., Wang, M., 2014a. Spatio-temporal distribution and tectonic settings of the major iron deposits in China: an overview. *Ore Geol. Rev.* 57, 247–263.
- Zhang, Z.C., Hou, T., Li, H.M., Li, J.W., Zhang, Z.H., Song, X.Y., 2014b. Enrichment mechanism of iron in magmatic-hydrothermal system. *Acta Petrol. Sin.* 30, 1189–1204 (in Chinese with English abstract).
- Zhang, Z.C., Santosh, M., Li, J.W., 2015. Iron deposits in relation to magmatism in China. *J. Asian Earth Sci.* 113, 951–956.
- Zhao, Y.S., 2000. Origin and geological properties of Cihai iron deposit, Xinjiang: Northwest. *Geology* 33, 31–38 (in Chinese).
- Zheng, J.H., Mao, J.W., Yang, F.Q., Liu, F., Zhu, Y.F., 2015. The post-collisional Cihai iron skarn deposit, eastern Tianshan, Xinjiang, China. *Ore Geol. Rev.* 67, 244–254.
- Zheng, J.H., Mao, J.W., Yang, F.Q., Chai, F.M., Liu, F., 2016a. Newly discovered native gold and bismuth in the Cihai iron-cobalt deposit, eastern Tianshan, Northwest China. *Acta Geol. Sin. (English Edition)* 90 (3), 928–938.
- Zheng, J.H., Chai, F.M., Yang, F.Q., 2016b. The 401–409 Ma Xiaodonggou granitic intrusion: implications for understanding the Devonian Tectonics of the Northwest China Altai orogen. *Int. Geol. Rev.* 58, 540–555.
- Zheng, J.H., Mao, J.W., Chai, F.M., Yang, F.Q., 2016c. Petrogenesis of Permian A-type granitoids in the Cihai iron ore district, Eastern Tianshan, NW China: constraints on the timing of iron mineralization and implications for a non-plume tectonic setting. *Lithos* 260, 371–383.
- Zheng, J.H., Chai, F.M., Yang, F.Q., Meng, Q.P., 2017. Geology, genesis, and geodynamic setting of Cihai: an Early Permian diabase-hosted skarn iron deposit in the eastern Tianshan, Northwest China. *Int. Geol. Rev.* <http://dx.doi.org/10.1080/00206814.2016.1258677>.
- Zhou, T.F., Yuan, F., Zhang, D.Y., Fan, Y., Liu, S., Peng, M.X., Zhang, J.D., 2010. Geochronology, tectonic setting and mineralization of granitoids in Juelutage area, eastern Tianshan, Xinjiang. *Acta Petrol. Sin.* 26 (2), 478–502 (in Chinese with English abstract).
- Zhu, Y.F., Guo, X., Song, B., Zhang, L.F., Gu, L.B., 2009. Petrology, Sr-Nd-Hf isotopic geochemistry and zircon chronology of the Late Paleozoic volcanic rocks in the southwestern Tianshan Mountains, Xinjiang, NW China. *J. Geol. Soc. London* 166, 1085–1099.
- Zhu, Y.F., An, F., Feng, W.Y., Zhang, H.C., 2016. Geological evolution and huge ore-forming belts in the core part of the Central Asian Metallogenic region. *J. Earth Sci.* 27, 491–506.
- Zürcher, L., Ruiz, J., Barton, M.D., 2001. Paragenesis, elemental distribution, and stable isotopes at the Peña Colorada Iron Skarn, Colima, Mexico. *Econ. Geol.* 96 (3), 535–557.